TAMPEREEN TEKNILLINEN YLIOPISTO
TAMPERE UNIVERSITY OF TECHNOLOGY

ARTTU LAITINEN

TWO-DIMENSIONAL SIMULATION OF THERMAL CUTTING OF LOW-ALLOYED STEELS

Master of Science Thesis

Examiners: Professor Arto Lehtovaara, Associate Professor Minnamari Vippola, Post-doctoral Researcher Matti Isakov
Examiners and topic approved in the Council of the Faculty of Engineering Sciences on June 3rd 2015

TIIVISTELMÄ

ARTTU LAITINEN: Niukkaseosteisten terästen termisen leikkaamisen kaksiuloitteinen simulointi
Tampereen teknillinen yliopisto
Diplomityö, 67 sivua, 4 liitesivua
Syyskuu 2015
Konetekniikan diplomi-insinöörin tutkinto-ohjelma
Pääaine: Laitossuunnittelu
Tarkastajat: Arto Lehtovaara, Minnamari Vippola, Matti Isakov

Avainsanat: Simulointi, Terminen leikkaus, Elementtimenetelmä, Niukkaseosteinen teräs, Jäännösjännitys

Polttoleikkaus on yleisesti käytetty termisen leikkauksen menetelmä, jossa paksuja teräslevyjä poltetaan kontrolloidusti liekin ja happisuihkun avulla aikaansaaden leikkausreunan. Liekin lämpöenergia aiheuttaa huomattavia lämpöeroja, jotka saavat aikaan plastisia muodonmuutoksia, faasimuutoksia ja jäännösjännityksiä teräslevyn sisälle. Jäännösvetojännityksien on oletettu olevan yksi polttoleikkauksen jälkeen tapahtuvan halkeilun aiheuttajista, jota tapahtuu leikattujen teräslevyjen varastoinnin yhteydessä.

Halkeilun estämiseksi on voitava perinpohjaisesti ymmärtää ja optimoida itse polttoleikkausprosessia. Tähän tarvitaan tietoa teräslevyn sisällä vallitsevasta tilasta, kun siihen kohdistetaan suuri määrä lämpöenergiaa. Lämpöhistoria on teräksen faasijaon määräävä tekijä, ja optimaalisen mikrorakenteen synnyttäminen on jokaisen lämpökäsittelyprosessin toivottu lopputulos. Tietoa teräslevyn lämpöhistoriasta ja jännitysjakaumista voidaan saada mallintamalla prosessi.

Työssä mallinnettiin niukkaseosteisen teräksen polttoleikkausta elementtimenetelmään perustuvalla ABAQUS-ohjelmalla. Ensin luotiin materiaalimalli, joka vastasi tutkitun niukkaseosteisen teräksen ominaisuuksia, jonka jälkeen austeniitti- ja martensiittifaasimuutokset sisällytettiin malliin aliohjelmien avulla. Leikkausliekki luotiin aikariippuvaisena lämpövuona, joka simuloi liekin liikkumista.

Mallia hyödynnettiin monin eri tavoin, kuten erilaisille leikkausnopeuksille, sekä eripaksuisille, esi- ja jälkilämmitetyille levyille. Työssä on esitetty kaikkien näiden käyttökohteiden tulokset, mutta työn päätulokset ovat 150 ja 300mm/min leikkausnopeuksien tuottamat lämpöhistoriat ja jäännösjännitykset. Näillä leikkausnopeuksilla saadut tulokset ovat rohkaisevia ja ne vastaavat kohtuullisella tarkkuudella mittaustuloksia. Jatkotutkimuksille on tarvetta mallin edelleen verifioimiseksi, sillä liekin mallintamiseen käytetty lähestymistapa poikkeaa jonkin verran aikaisemmissa tutkimuksissa käytetyistä keinoista.

ABSTRACT

ARTTU LAITINEN: Two-dimensional simulation of thermal cutting of low-alloyed steels
Tampere University of Technology
Master of Science Thesis, 67 pages, 4 Appendix pages
September 2015
Master's Degree Programme in Mechanical Engineering
Major: Design of Machine Systems
Examiners: Arto Lehtovaara, Minnamari Vippola, Matti Isakov

Keywords: Simulation, Thermal cutting, Finite elements, Low-alloyed steel, Residual stress

Flame cutting is a commonly used method of thermal cutting, where a controlled flame and oxygen jet are applied to a thick steel plate to burn it and to create a cut edge. This heat from the flame causes significant temperature differences, which induce plastic deformation, phase transformations and residual stresses inside the steel plate. Tensile residual stresses are assumed to be a factor in delayed cracking, which happens when the steel plates are put into storage.

To thoroughly understand and optimize the flame-cutting process for preventing the cracking, more information about the conditions inside the steel plate, while it is being applied with a large amount of heat, is needed. Temperature history is the defining factor to the phase distribution of steel, and creating an optimal microstructure is the desired outcome of every heat-treatment process. By modelling the process, more information about the stress distribution and the temperature history can be obtained.

A model of flame-cutting of low-alloyed steel was made by using a commercial finite element program ABAQUS. First the material was created to resemble the characteristics of the studied low-alloyed steel, and then the austenite and martensite phase transformations were introduced to the model by user subroutines. The cutting flame was created as a time-dependent heat flux to simulate the movement of the flame.

The model was used for various applications, such as different cutting speeds, flame-cutting of steel plates with different thicknesses, pre-heating and post-heating. The results of all these applications are presented, but the main subjects of the study are the temperature history and residual stress results from the cutting speeds of 150 and 300mm/min. The results obtained from these cutting speeds are encouraging and correspond relatively well with the experimental results. Further study is needed to completely verify the model, as the approach to the modelling of the flame is slightly different from earlier studies.

PREFACE

This thesis was carried out at the Faculty of Materials science, Tampere University of Technology, during the years 2014-2015, and was financed by SSAB.

I'm extremely grateful to all the people who helped me during this challenging yet rewarding work. First I want to thank Professor Arto Lehtovaara and Associate Professor Minnamari Vippola for supervising this project in a motivating manner, and for their insight regarding the structure and content of this thesis.

I am deeply grateful to Dr. Matti Isakov for mentoring me throughout the whole process and having time to help me whenever it was needed. Also the help with processing the yield strength measurement data was gladly received.

Also I would like to express my appreciation to Tuomo Saarinen from SSAB, who provided the subject and gave his insight to the objects of this thesis. Also the interest he showed towards this thesis was well motivating, which translated into a great result.

Thank you to M.Sc. Tuomas Jokiaho for providing me the residual stress measurement results used in this thesis, and for the discussions with Dr. Isakov, which were extremely helpful.

Juha Uusitalo from the University of Oulu deserves my gratitude for conducting the Gleeble-measurements and providing the yield strength data used in the model.

Finally I want to thank my family and friends who have been supporting me through all these years. A special thank you goes to my good friend M.Sc. Matti Lindroos, who suggested me to apply for this job, and helped me solve some of the problems I had regarding the simulations.

This has been an extremely educating process, but I am glad it is finally over, for now.

Tampere, 22.9.2015

Arttu Laitinen

TABLE OF CONTENTS

1. INTRODUCTION 1
2. THERMAL CUTTING 2
2.1 Flame-cutting 2
2.2 Plasma arc cutting 4
2.3 Laser cutting 5
3. MATERIAL MODELLING 6
3.1 Material properties 7
3.1.1 Thermal conductivity 7
3.1.2 Heat capacity 8
3.1.3 Density 9
3.1.4 Thermal expansion 10
3.1.5 Young's modulus 11
3.1.6 Poisson's ratio 12
3.1.7 Yield strength 14
3.1.8 Thermal boundary conditions 16
3.2 Phase transformations 17
3.2.1 Austenite 17
3.2.2 Martensite 21
3.3 Stress analysis 23
3.3.1 Residual stress 26
3.3.2 Residual stresses induced by flame-cutting 26
3.3.3 Finite element approach on stresses 29
4. THERMOMECHANICAL ANALYSIS 33
4.1 Modelling of flame-cut steel plate 33
4.1.1 Meshing the part 33
4.1.2 Modelling of low-alloyed steel 35
4.1.3 User subroutines 38
4.2 Flame modelling 41
5. RESULTS AND DISCUSSION 45
5.1 Temperature 45
5.2 Residual stresses 49
5.3 Model verification against experiments 59
6. CONCLUSION 63
REFERENCES 65

APPENDIX A: USER SUBROUTINE CODE

ABBREVIATIONS AND NOTATION

ABAQUS	FEM (Finite element method) simulation program
BCT	Body-centered tetragonal
CCT	Continuous cooling transformation
FCC	Face centered cubic
FEM	Finite element method
FIELD(X)	Field variable
GETVRM	ABAQUS utility routine
HAZ	Heat affected zone
JMatPro	Thermal calculation program
LBC	Laser beam cutting
OFC	Oxygen or oxyfuel gas cutting
PAC	Plasma arc cutting
SEM	Scanning electron microscope
STATEV(X)	State variable
TTA	Time-Temperature-Austenitization
TTT	Time-Temperature-Transformation
UEXPAN	ABAQUS subroutine
USDFLD	USER DEFINED FIELD ABAQUS subroutine

A	Surface area
A_1	Austenite start temperature
A_3	Full austenite temperature
C_i	Principal tensor invariants
c_p	Specific heat
E	Young's modulus
$\mathbf{F}$	Force
f_i	Phase fraction
h	Enthalpy
h_c	Heat transfer coefficient
$\mathbf{I}$	Internal force
[K]	Stiffness matrix
L	Length
m	Mass
M_f	Martensite finish temperature
M_s	Martensite start temperature
$\mathbf{n}$	unit vector
$\mathbf{P}$	External load
p	Pressure
p_i	Body force
Q	Heat flow
q_c	Convective heat loss
q_r	Radiative heat loss
R_i	Residual vectors
$[S]$	Stress matrix
S_{22}	Vertical residual stress
T, θ	Temperature

T_{max}	Maximum temperature
t	Time
$t_{\alpha i}$	Stress tensor
$\{u\}$	Displacements
[V]	Strain matrix
V	Volume
x_i	Axial length
α	Thermal expansion coefficient
ε_i	Strain
ε	Emissivity
λ	Thermal conductivity
ν	Poisson's ratio
ρ	Density
σ_{ii}	Normal stress
σ	Stefan-boltzmann constant
τ_{ij}	Shear stress

1. INTRODUCTION

Thermal cutting of steel is a heat treatment process, where a steel plate is being subjected to a large amount of concentrated heat and the applied part of the steel plate melts or vaporizes away. Thermal cutting is an exothermal process, which means that the burning process maintains itself with less heat required. Flame-cutting is the most common method of thermal cutting used in the steel industry, because it is quite cost-efficient and it can be applied to thick steel plates.

Understanding of flame-cutting from a mechanical and thermal point of view has been a continuous matter of interest in the steel industry. This is because cracking has been a recurring incident involved with flame-cutting, which naturally is not a desired outcome, as it causes production losses. Because of the conditions involved in flame-cutting, physical measurements are extremely hard to conduct. Especially stress measurements are close to impossible to perform, but temperature measurements can be done, although the results are highly sensitive to the measuring arrangements. Residual stresses are the commonly used subject of stress analysis, but there is a need for more diverse research.

The aim of this thesis is to give answers to the following questions: what happens to steel while it is being flame-cut? What is the magnitude of the stresses, which are induced by the temperature differences inflicted by the cutting flame? The chosen research method for finding the answers is modelling. The model will be made by using a commercial program called ABAQUS, which uses the finite element method and is suitable for thermomechanical calculations. Phase transformations occur as the steel plate is subjected to high temperatures, and understanding the mechanics behind these transformations is also one of the objectives for this study, and including them into the model is extremely desired.

This thesis consists of theory part, where different methods of thermal cutting are discussed. Also the material properties and phases of steel, that are significant for the model, are included. Stress analysis concludes the theory part of the thesis. Following is a chapter about creating the model; what needs to be taken into consideration when flame-cutting is simulated. Results and discussion are then presented in chapter 5 and finally, conclusions and final remarks are found in chapter 6.

2. THERMAL CUTTING

Different methods of thermal cutting are presented in this chapter. The methods at issue are flame-cutting, plasma arc cutting and laser cutting. These methods have their own attributes, making them suitable for specific applications. The pros and cons of each method are listed and the theories behind the processes are discussed, with flame-cutting being the main objective.

2.1 Flame-cutting

Also known as oxygen or oxyfuel gas cutting (OFC), flame-cutting is one of the most commonly used cutting methods in steel industry due to OFC's low cost and high precision cuts. It is a process that utilizes a combination of a controlled flame and an oxygen jet to cut and remove molten steel to create a precise edge. Flame-cutting can be used to cut through thick plates up to 1500mm. [1][2]

During flame-cutting the metal is first heated to its ignition temperature with a primary flame and then the oxygen jet is introduced to create a chemical reaction that melts the steel. This chemical reaction is the oxidation of steel, and it is continuous, so it will help the melting process to proceed further with less heat input. This is achieved because oxidation process is exothermal, which means that it releases heat during the process. Excess molten steel is removed by the high-velocity oxygen jet so that mainly a clear-cut edge remains. [3]

In conclusion flame-cutting is based on metal oxidation and removal of metal oxide that has reached molten state. The principle of flame-cutting is presented in figure 2.1. Heat generated by the heating flame and the exothermal reaction needs to be sufficient to replace the heat loss accumulated by radiation, conduction, convection and removal of molten metal oxide. Heating flame must bring enough heat to the upper part of the cut, where heat losses are the greatest and the metal oxide is not yet formed. [3]

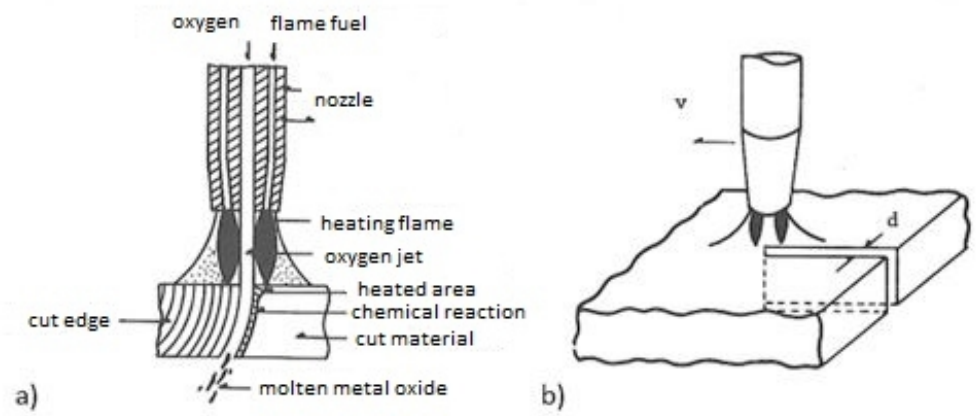

Figure 2.1. *Principle of flame-cutting. In figure b) v is the cutting speed and d is the cutting width. [3]*

There are some advantages and disadvantages when using flame-cutting, and here is a list of the former:

- Various shapes that are difficult to produce mechanically can be produced cost-efficiently with flame-cutting. [1]
- Required equipment and operating costs are relatively cheap. [3]
- Cut quality is excellent with right cutting parameters. [3]
- Cutting speed is not as thickness dependent as with other thermal cutting methods. [3]
- The movability of the cutting torch enables to cut large plates that are fixed. [1]
- Cutting direction can be changed quickly. [1]
- Increase of hardness on the cut surface is relatively small. [3]

Disadvantages considering flame-cutting are important to acknowledge, since they are often decisive when choosing which thermal cutting method to use. Here are some of those disadvantages listed:

- Flame-cutting is generally limited to cutting steels and cast iron. [1]
- Some modifications to the process must be made to cut high alloy steels and cast irons [1]
- To control metallurgical and mechanical properties near the cut edge, preheating and post heating might be required [1].
- Heat affected zone (HAZ) is wide compared to other thermal cutting methods. [3]
- Cutting speed is low while cutting thin, under 20mm, plates.
- Method is not suitable for cutting small and complicated shapes. [3]

To be able to cut with OFC, the material must meet some criteria. Prerequisites for material's usability in flame-cutting are as follows:

- Material must burn with oxygen. [3]
- Thermal conductivity must be as low as possible to reach high combustion heat. [3]
- Ignition temperature of the material must be lower than its melting temperature, otherwise work piece would melt. [3]
- Melting temperature of the metal oxide must be lower than materials. [3]
- Combustion reaction must generate enough heat to maintain material's ignition temperature through the whole process. [3]
- Viscosity of the molten metal oxide must be low, so that it can be easily removed from the cut. [3]

2.2 Plasma arc cutting

Plasma arc cutting (PAC) is a cutting method that uses extremely hot plasma gas that melts and partially vaporizes work piece material. This plasma gas jet is formed by an arc and inert gas flow. Plasma arc is concentrated with a nozzle to create more precise and even hotter arc, that operates approximately at 10 000 – 14 000 °C. Molten material is removed by the high velocity gas jet, much like in OFC. [1] [3]

Plasma arc is created by heating gas with an arc. This gas then becomes partially ionized thus being able to conduct electricity. Heating the gas rapidly as it travels along the arc makes it expand. Then the gas is accelerated through the nozzle towards the work piece. Gases used in plasma cutting include nitrogen, argon, air, oxygen and mixtures of nitrogen/hydrogen and argon/hydrogen. This thesis' material, low-alloyed carbon steel, is a very suitable material to be cut with PAC. [1]

To evaluate plasma arc cutting as a process, it is beneficial to also compare it to other thermal cutting methods. Here are some benefits compared to flame-cutting:

- Plasma arc cutting is suitable for metals that can't be cut with flame-cutting [3]
- Higher cutting speeds with thin plates. [4]
- Heat affected zone is smaller [3]
- Narrow cut and low dross formation. [4]

Disadvantages when using plasma arc cutting:

- High cost of equipment and cutting requires a lot of energy [3]
- Cutting speed decreases drastically when material thickness grows. Maximum thickness that can be cut with PAC is approximately 120mm. [3][4]
- High environmental protection costs. [4]
- Hardness on the cutting surface can grow substantially. [4]
- Cutting surfaces can be a bit skewed. [4]

2.3 Laser cutting

Laser beam cutting (LBC) is a thermal heating method that creates cutting kerfs by melting and vaporizing material with a concentrated coherent light beam. The process is thermal heating and the input power must exceed all heat losses that occur. Best cut quality is achieved when the intensity of the energy absorbed by the cut material is very large. Parameters for the intensity of energy are laser output power, beam diameter and the absorption coefficient, which means the fraction of light absorbed by the cut. [1]

Out of all thermal cutting methods, laser cutting has the smallest thermal effects on the cut material. This means smaller heat affected zone and a narrower kerf. Also distortion is almost nonexistent. The above mentioned added with a small steady laser beam enables very high velocity cutting. With thin plates, laser cutting has replaced mechanical cutting as main method. Laser cutting can be used to cut non-metals as well and it is very adaptable due to computer controlled contour cutting. [4]

The reason why laser cutting is not applied in every facility is the capital cost of equipment and it’s impracticality in cutting through plates thicker than 13mm [1]. Also deviation of the laser beam can cause dangerous situations. These situations may occur while cutting highly reflective surfaces, for example bright aluminium plates [4].

Different kinds of thermal cutting methods were introduced in this chapter. In this work the main focus is on the phenomena that happen inside the steel plate. Though all of the introduced processes are very different from each other, the thermal impact that they have on the applied part is relatively similar, which is a very large amount of concentrated heat that melts or vaporizes the material. Therefore the modelling will focus on flame-cutting, instead of including all of the presented methods.

3. MATERIAL MODELLING

Material behavior of steel is highly dependent on its chemical composition. In this thesis the composition being used is an approximation of the steel produced by the customer. Same composition was used in reference [2] and it is presented in table 1. This composition was used as an input for a thermal calculation program called JMatPro, which generated several material parameters and graphs that were utilized in creating the model. JMatPro is a program that incorporates theoretical material models with property databases and uses them to calculate requested parameters [35].

Also a yield strength measurement was conducted in the University of Oulu to improve the result of the simulation in stress calculations. Some of the properties were taken from literature.

Table 1. *Chemical composition approximation of the surveyed steel. [2]*

	C	Si	Mn	P	S	Al	Nb	V
Weight %	0,132	0,617	0,969	0,009	0,0007	0,081	0,003	0,037
	Cu	Cr	Ni	N	Mo	Ti	Ca	B
Weight %	0,012	0,887	0,058	0,0027	0,27	0,013	0,002	0,0014

In the model both thermal and mechanical properties are assumed to be the same throughout the whole part, except for thermal and phase-induced expansion, which was determined by the phase composition of the part and entered into the model with user subroutines. This is presented in subsection 4.1.3. With the help of user subroutines, different material properties could also be assigned whether the part is heating up or cooling down.

These different material properties of steel, and the theory involving them, are presented in the following section. A section of the phase transformations that are assumed to occur during the flame-cutting process and the characteristics of these phases is also included. The chapter is finally concluded with a mechanical approach, which introduces the methods and theories used to calculate the stresses and strains induced by the flame-cutting process.

3.1 Material properties

In order to get valuable data out of the simulation, special attention must be directed to the material properties of the steel. The material behavior in the simulation needs to be as similar as possible with real life events of thermal cutting. It is evident that with large amount of different parameters and extremely high heating and cooling rates, not everything can be exact. But with sufficient accuracy on the relevant material properties, usable data can be simulated.

3.1.1 Thermal conductivity

Thermal conductivity, λ, is heat transfer through material without material flow. It describes the ability of material to conduct heat from high-temperature region to low-temperature region [8].

Conduction heat transfer is described by Fourier's law in one-dimensional case:

$$Q = -\lambda \frac{dT}{dx} At \tag{3.1}$$

where Q is the heat transferred, λ is the thermal conductivity, A is the area projected by the heat flow, t is the time and dT/dx is the temperature gradient. [8]

In the present work, thermal conductivity has a large impact on the thermal analysis, so it is needed to be entered into the model as accurately as possible. Values for thermal conductivity used in the model are presented in figure 3.1.

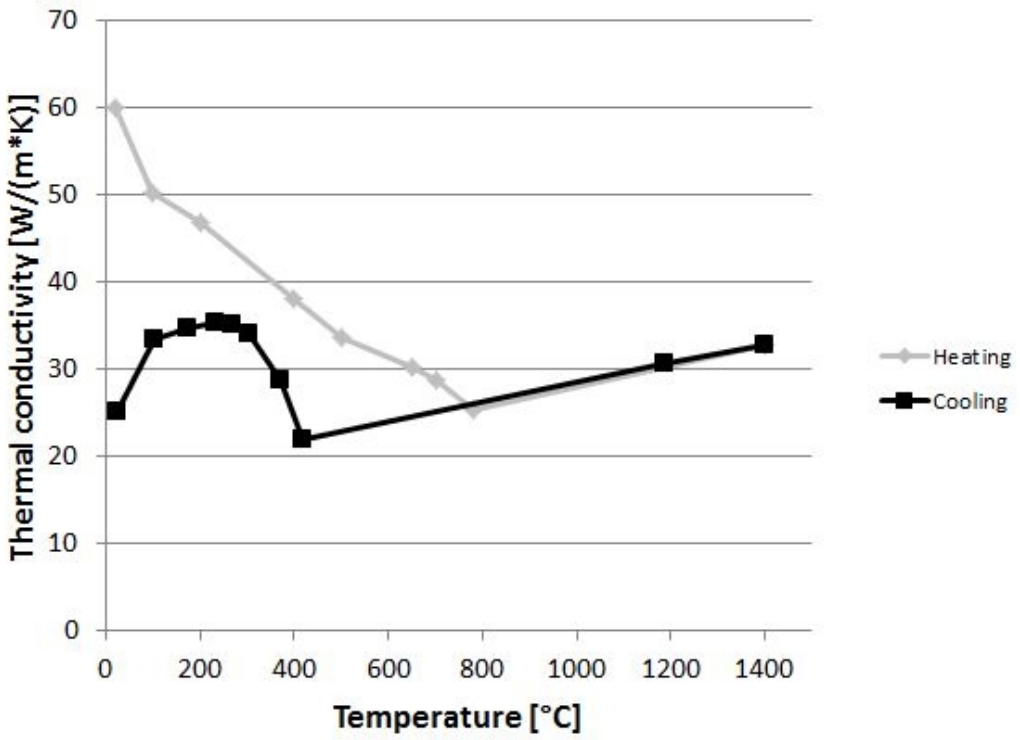

Figure 3.1. *Thermal conductivity of the studied steel as a function of temperature. Based on numerical results from JMatPro.*

As can be seen from the figure above, there is a difference between the graphs in lower temperatures. This is a result of the phase transformations that occurs in the steel during the thermal cutting process.

3.1.2 Heat capacity

Heat capacity is described as a relation between the quantity of heat brought in to the system and the temperature increase induced by this heat. In other words heat capacity is a material property that measures the ability of the material to store heat. Specific heat, c_p, is used as an input in the model and it is heat capacity measured in constant pressure. [9]

Specific heat is defined using state variable enthalpy, h, which is defined as the sum of internal energy added with a product of pressure and volume. Specific heat is defined as

$$c_p = \left(\frac{dh}{dT}\right)_p \tag{3.2}$$

Specific heat is always strongly temperature dependent. This is a result of molecules and atoms having more degrees of freedom to increase the internal energy due to the rise of temperature. [9]

The relation between the heat energy input and the temperature change in the material can be simplified into an approximation defined as

$$Q_{12} = mc_p dT \tag{3.3}$$

where m is the mass. [7]

Equation 3.3 is an approximation and will not be used in calculations for the model, but it is presented to describe the effect that specific heat has in thermal analysis. Input values for specific heat applied in the simulation were generated using JMatPro and they are presented in figure 3.2 for both heating and cooling.

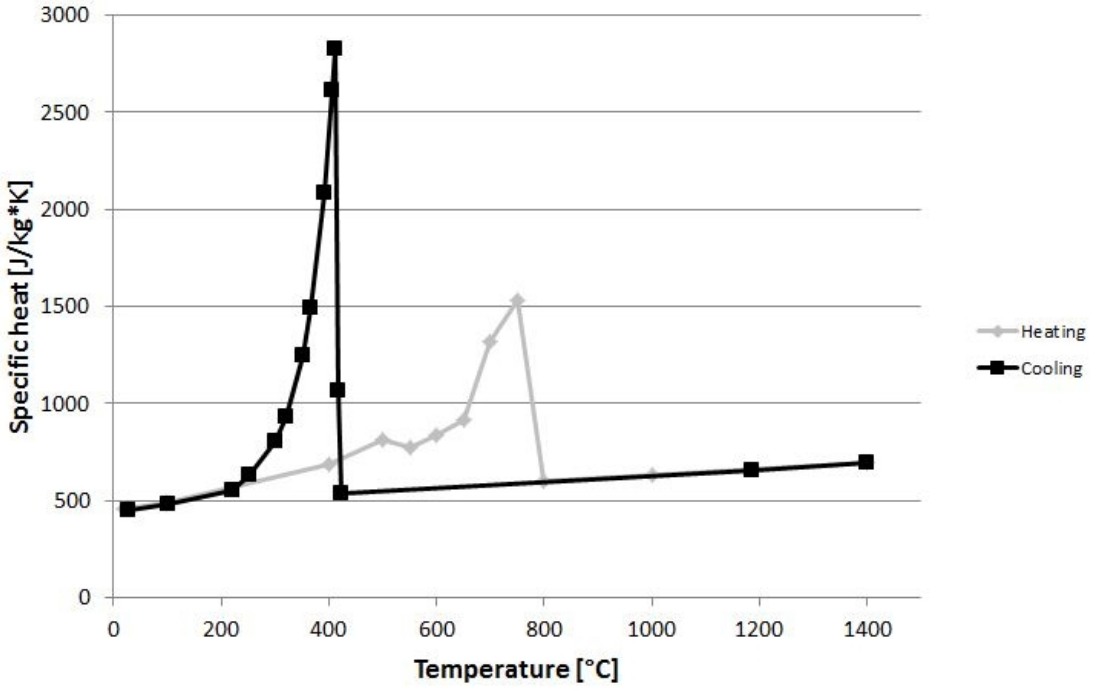

Figure 3.2. *Specific heat as a function of temperature. Based on numerical results from JMatPro.*

As already noted, sudden increases in the values of specific heat, as can be seen in figure 3.3, are results of phase transformations happening in the steel during the thermal process. Phase transformations at issue are austenitic and martensitic transformation, and they are more specifically discussed further in section 3.2.

3.1.3 Density

Density is a material property, much like heat capacity, that is used in thermal analysis to calculate the heat storage in the material. For simulation with common steels, it can often be assumed temperature independent [7]. In this case the density is assumed temperature dependent and the values decrease evenly from room temperature to melting temperature [14]. This is presented in figure 3.3.

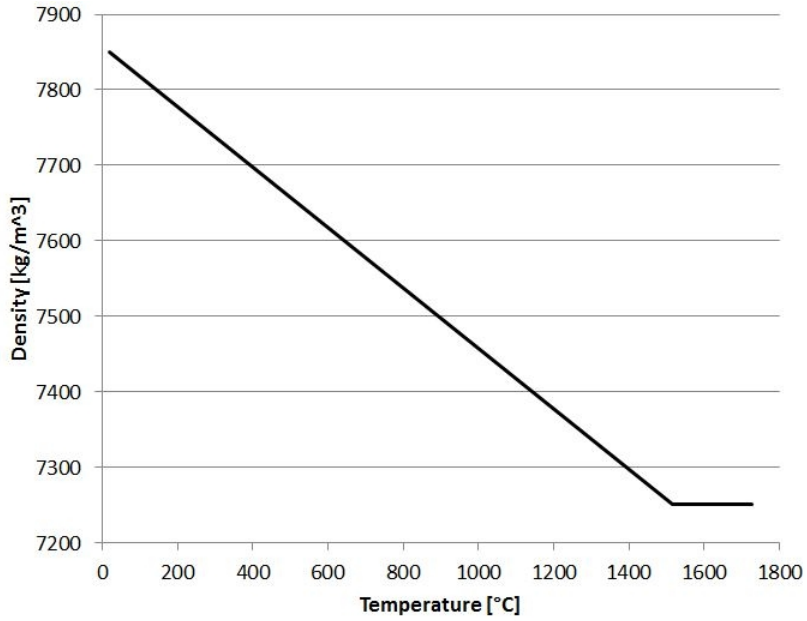

Figure 3.3. *Density as a function of temperature.*

Density is not very important variable in the simulation from mechanical analysis point of view [7]. This is because in the model the part is fully supported from the bottom and therefore gravity has negligible effect on the stress gradient (no bending).

3.1.4 Thermal expansion

According to thermal laws, when material is being subjected to temperature change, it either contracts or expands, depending on the direction of the change in the temperature gradient. This kind of behavior is called thermal dilatation and the unit used to measure it is coefficient of thermal expansion, α. Thermal expansion is the most significant material property when surveying the contribution that thermal load has on the mechanical system, because it affects the stress-gradient of the surveyed part. [7,12]

Thermal strains can be calculated using the thermal expansion coefficient. In Abaqus the thermal strains are defined as

$$\varepsilon_{th} = \alpha(T, f_\beta)(T - T_0) - \alpha(T_I, f_\beta^I)(T_I - T_0) \tag{3.4}$$

where $\alpha(T,f_\beta)$ is the thermal expansion coefficient, T is the current temperature, T_I is the initial temperature, f_β are the current values of the predefined field variables, f_β^I are the initial values of the field variables and T_0 is the reference temperature for the thermal expansion coefficient. [13]

In the simulation the reference temperature and the initial temperature are the same, so only the first term of equation 3.4 will be used.

The values for the thermal expansion coefficient in the model are determined according to the temperature gradient of the elements and whether they reach the phase transformation temperatures. For martensitic steel the coefficient was set to 13 x 10^{-6} 1/K at room temperature and increasing with temperature and for full austenitic steel the coefficient was set to 20 x 10^{-6} 1/K. For dual-phase area the coefficient was set according to the phase proportions of the element.

One of the objectives of this thesis was to simulate the phase transformations as well, therefore in addition to thermal expansion, the expansion subroutine (UEXPAN) also includes a variable for phase transformation induced expansion, which will be presented in subsection 4.1.3. The values for the thermal expansion coefficient were validated by comparing them with the results from dilatometer tests conducted at the University of Oulu. These measurements were conducted at the same time with the yield strength measurements.

3.1.5 Young's modulus

Elastic behavior of the material is an essential attribute for conducting a proper stress analysis on the surveyed part. It indicates the ability of the material to resist non-permanent deformation when a load is applied on it. A quantity for this ability is Young's modulus, E, and it indicates the ratio between stress and strain, as defined by one-dimensional Hooke's law as [7, 12]

$$E = \frac{\sigma}{\varepsilon} \tag{3.5}$$

where σ is the tensile stress and ε is the extensional elastic strain.

Young's modulus is normally measured in a uniaxial test, but this was not an option for this study, so the values were generated, much like for many of the thermal properties, by using JMatPro. These values are presented in figure 3.4.

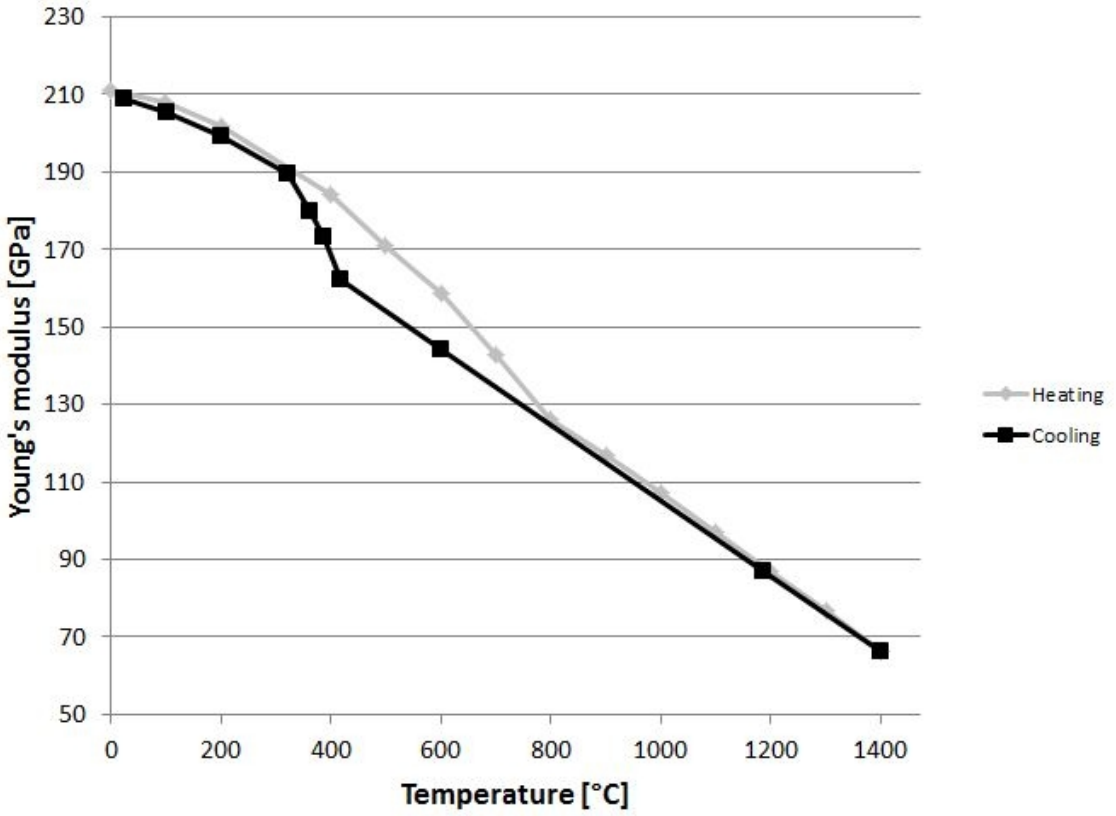

Figure 3.4. *Young's modulus as a function of temperature. Based on numerical results from JMatPro.*

As can be seen from figure 3.4, the elastic modulus of the material steadily decreases while the temperature increases. The deviation in the cooling curve approximately at 700K is a result of the martensitic transformation which starts at this temperature. Graphs were compared with the graphs presented in other references [7, 11] and a good correspondence was found.

3.1.6 Poisson's ratio

It is experimentally proven, that in addition to longitudinal strain, there is transverse expansion in a compressed beam. This kind of elastic deformation can be predicted using Poisson's ratio, ν, that is a variable that measures the relation between the lateral strain, $\varepsilon_{\perp}$, and axial strain, ε, defined as [12]

$$\nu = -\frac{\varepsilon_{\perp}}{\varepsilon} \tag{3.6}$$

Because lateral strain and axial strain are generally of opposite sign, negative sign is included in the equation. [16]

Normally Poisson's ratio for steels at room temperature locates between 0.27 and 0.30 [12]. For the studied steel this was also true, but for the simulation to be accurate in the

analysis, values needed to be temperature dependent. Using JMatPro, values could be created as shown in figure 3.5.

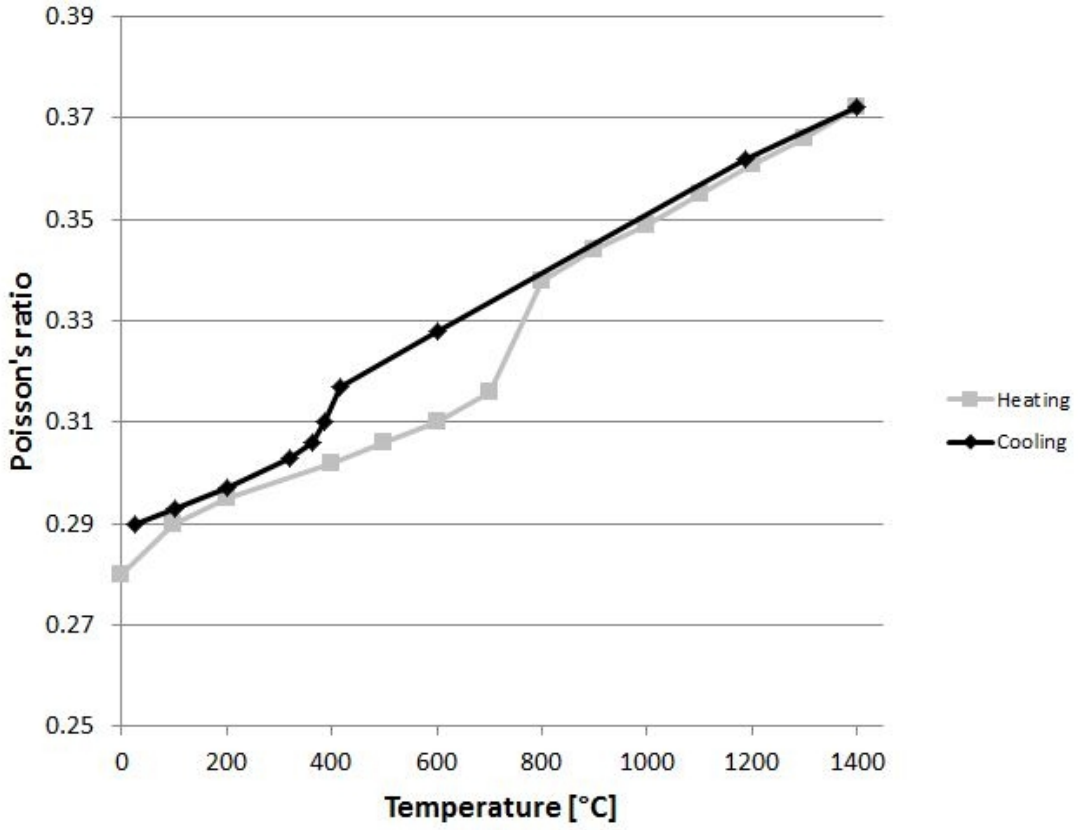

Figure 3.5. *Poisson's ratio as a function of temperature. Based on numerical results from JMatPro.*

To further explain the effect of Poisson's ratio and Young's modulus on the elastic behavior of the material, some equations are provided. The generalized Hooke's laws state that for isotropic and linearly elastic materials, elastic axial strains for x-, y- and z-directions can be defined as [12]:

$$\varepsilon_x = \frac{1}{E}[\sigma_x - \nu(\sigma_y + \sigma_z)] \tag{3.7a}$$

$$\varepsilon_y = \frac{1}{E}[\sigma_y - \nu(\sigma_x + \sigma_z)] \tag{3.7b}$$

$$\varepsilon_z = \frac{1}{E}[\sigma_z - \nu(\sigma_x + \sigma_y)] \tag{3.7c}$$

where σ_i are the normal stresses in the x-, y- and z-directions.

As can be seen from the equations above, the elastic axial strain in one direction is affected by the normal stresses in the other directions via Poisson's ratio. Vice versa, the strain in one direction may induce stresses in the transverse directions depending on the strain boundary conditions.

3.1.7 Yield strength

Plasticity of a material is an extremely important factor in stress analysis. Yield strength is considered as the basic quantity for plasticity and it measures the stress needed to create permanent deformation in the material. For calculation, yield strength is defined from the stress-strain curves of the material. [7]

Exact point of yielding is often hard to define from the stress-strain curves because of the shape of the curve. To reduce the inaccuracies, an offset yield point is arbitrarily defined [7]. Using this method the yield strength can be determined using the proportional limit of plastic strain as shown in figure 3.6. For the model the percent offset was selected to be 2% in order to minimize the effect of experimental uncertainty at small strains.

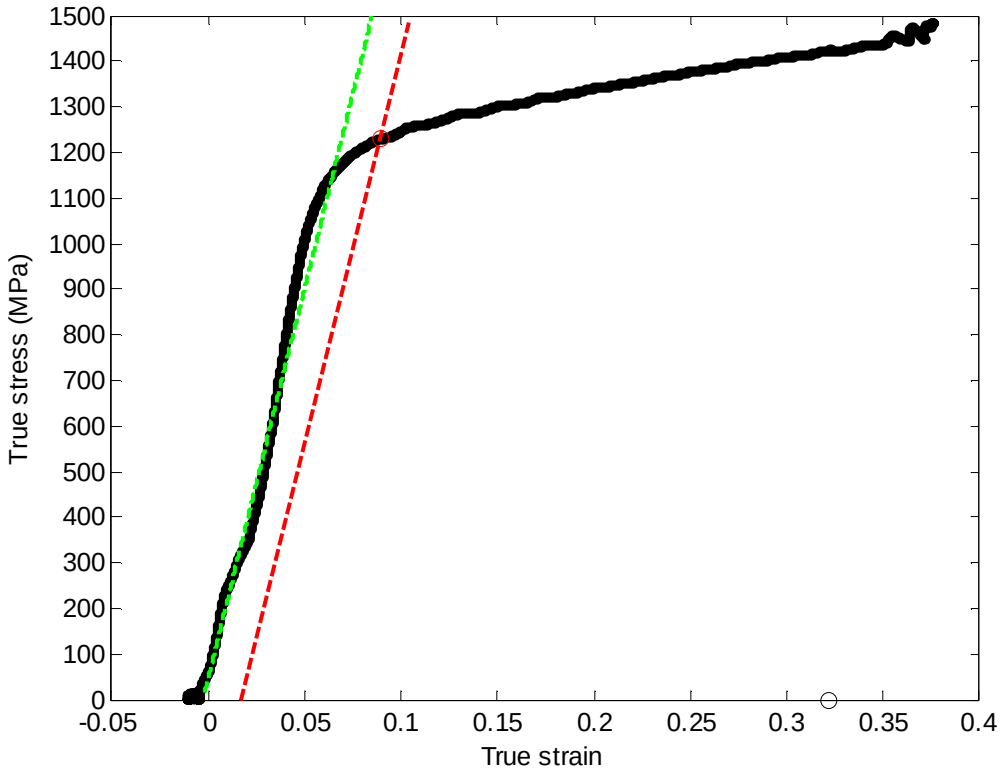

Figure 3.6. *Stress-strain curve to define the yield strength of the surveyed steel at room temperature. Based on the measurements conducted at the University of Oulu.*

Stress-strain curve presented in figure 3.6 is a result from measurements conducted at the University of Oulu. In figure 3.6, the green line is the linear fit on the elastic region and the red line is the offset line used to determine the yield strength. Black circle on the x-axis (around 0.32) is the strain that was measured manually after the test. The measurements were uniaxial compression tests performed by Gleeble 3800 thermo-mechanical simulator. The strain rate in the test was set to $1s^{-1}$ to correspond to the actual flame-cutting process. The specimen was heated to the target temperature with a

heating rate of 250°C/s and the loading was applied 0,5-1,0 seconds after reaching the target temperature. This was done to minimize the long-term effects of high temperatures to the material, such as tempering of martensite. Using the output data provided by the measuring device, which were applied force and change of length, true stress and true strain could be calculated as following:

engineering stress, σ_E, is defined as

$$\sigma_E = \frac{F}{A_0} \tag{3.8}$$

where F is the applied force and A_0 is the initial area perpendicular to the force.

Engineering strain, ε_E, is defined as

$$\varepsilon_E = \frac{\Delta L}{L_0} \tag{3.9}$$

where L_0 is the initial length of the measured part parallel with the applied force.

Equations for true stress, σ_T, and true strain, ε_T, could be derived using equations 3.8 and 3.9 and assuming that the material volume is constant in plastic deformation. For true stress the equation is as stated

$$\sigma_T = \frac{F}{A} = \sigma_E * (1 + \varepsilon_E) \tag{3.10}$$

and for true strain it is

$$\varepsilon_T = \int_{L_0}^{L} \frac{dL}{L} = \ln(1 + \varepsilon_E) \tag{3.11}$$

A series of tests were conducted in various temperatures to create a temperature-dependent yield strength graph by combining the results. This graph is presented in figure 3.7. It is worth mentioning that the stiffness of the measuring equipment was taken into account while calculating stress-strain graphs like in figure 3.6. This was done by compressing the gauge without a sample to determine the deformation of the machine as a function of load.

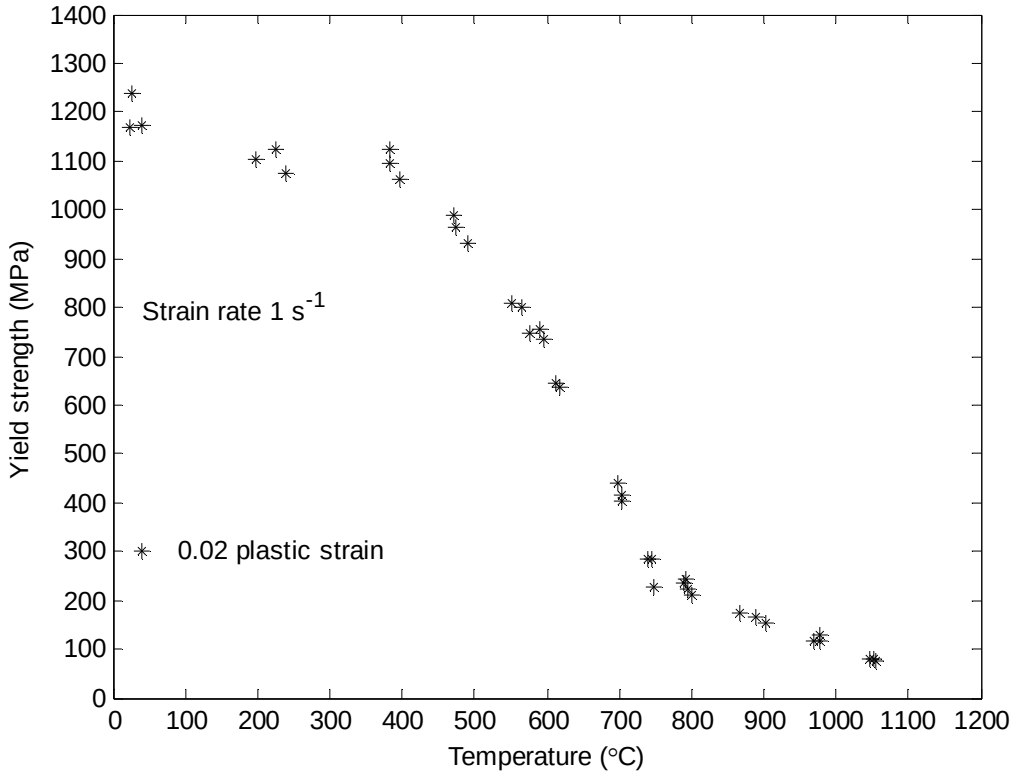

Figure 3.7. *Yield strength at 2% plastic strain as a function of temperature. Results are based on the measurements conducted at the University of Oulu.*

As can be seen from figure 3.7, yield strength is a highly temperature dependent material property. There is a significant drop in the values after temperature rises over 400°C. Acquiring correct values for yield strength as a function of temperature is important, because the yield limit is the variable that decides whether the material reacts elastically or elastoplastically, which has a major impact in the stress distribution inside the steel plate. It should be noted that the values for yield strength in figure 3.7 are for the heating stage only.

3.1.8 Thermal boundary conditions

Temperature differences are the main source of stress development inside the part, and in flame-cutting, the temperature distribution near the cut surface is immensely differential. In the thermal process, heat is transferred through the part by conduction, and after long enough time, all heat energy leaves the part through the boundaries. The conditions of these boundaries need to be properly predicted for the thermal distribution calculations to be precise. These boundary conditions used in the thermal analysis of flame-cutting are ambient, or prescribed, temperature, surface convection, q_c, and surface radiation, q_r. Surface heat flux can also be considered as a boundary condition, but it is further discussed in chapter 4.2. [7, 13]

The calculation of convective heat loss can be done by using the following equation:

$$q_c = h_c \cdot (T - T_0) \tag{3.12}$$

where h_c is the heat transfer coefficient and T_0 is the ambient temperature. The heat transfer coefficient depends on the surrounding conditions, such as air speed near the surface. [7]

The heat loss due to radiation can be defined by Stefan-Boltzmann's law as:

$$q_r = \varepsilon \cdot \sigma \cdot ((T + T_z)^4 - (T_0 + T_z)^4) \tag{3.13}$$

where ε is the emissivity constant, σ is the Stefan-Boltzmann constant and T_z is the absolute zero on the scale being used. [13]

3.2 Phase transformations

Steel is a highly versatile material and can be used for many tasks, but there is no steel, that is suitable for everything. This is why the mechanical characteristics of the steel must be valid for the task in hand. One of the methods to develop these characteristics to more desirable values is by altering the microstructure of the steel via heat treatment. While steel is being subjected to heat, phase transformations occur depending on the time and temperature of the subjected part. Different phases of steel have unique mechanical characteristics, and they can be produced by knowing the phase diagram of the steel at issue. Phase diagrams are diagrams that represent the temperature (equilibrium diagrams) or time-temperature (TTT and CCT) dependencies of the phases of the steel. For example, in [16] the tensile strength of a specific iron-carbon alloy was reported to vary between 700MPa and 2000MPa depending on the applied heat treatment.

In this chapter, two of the steel phases and their transformations will be discussed. These two phases at issue are austenite and martensite. Austenite forms in higher temperatures while the steel is being heated and martensite forms when the steel is cooling down at a specific cooling rate range.

3.2.1 Austenite

Austenite is a microstructural phase of steel, which forms by diffusion in high temperatures in low-alloyed steels. It is considered to be an intermediate phase, which in low-alloyed steels transforms to other more stable phases as the material temperature decreases. Formation of austenite is called austenitization, a process where the steel is heated to high temperatures to induce a polymorphic transformation into a crystal microstructure that is face-centered cubic (FCC) form. This structure is shown in figure 3.8. [23]

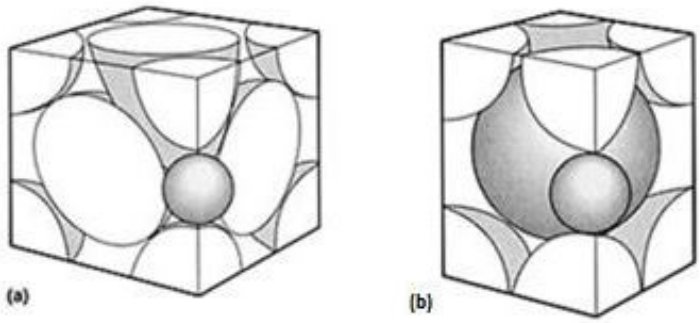

Figure 3.8. *Crystal structures of a) austenite (FCC) and b) martensite (BCT). The small sphere represents an interstitial carbon atom within the iron lattice. [17]*

By heating the steel into austenite phase field, a reaction occurs where austenite replaces the starting microstructure, which may include ferrite, bainite, pearlite, iron carbide, cementite, martensite or even austenite from previous processes. This kind of austenite is called retained austenite, and it is a result of incomplete phase transformation/decomposition. [23]

Phase transformations that happen by diffusion generally follow an S-shaped curve that depicts the volume fraction of the phase as a function of temperature and time, and austenite is no exception. The curve is normally generated using the Avrami equation, which is presented in equation 3.14 [16]. The mechanisms of austenite formation depend on the composition of the steel. Generally the austenite formation is more rapid in alloys with higher carbon content. The main processes happening in austenitization as the temperature increases are bulk formation of austenite, grain growth, carbide dissolution, homogenization of composition on a microscale and recrystallization. [24]

$$y = 1 - \exp(-kt^n) \tag{3.14}$$

where y is the volume fraction of the phase, t is time and k and n are time-independent constants whose values depend on the particular reaction. [16]

Study of austenite formation is often started with the iron-carbon equilibrium diagram, presented in figure 3.9, which illustrates the relations of different phases (γ for austenite, α for ferrite and Fe_3C for cementite) to temperature and carbon content. Although the diagram is for a simple binary Fe-C system, it gives a proper foundation to further examine the behavior of more complex alloy steels. [18]

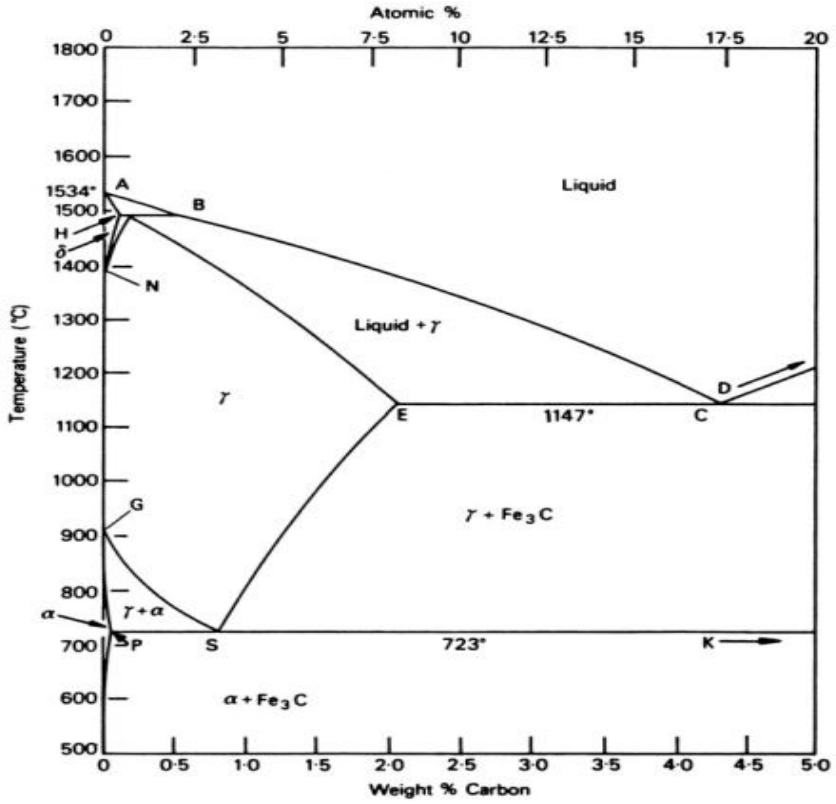

Figure 3.9. *The iron-carbon equilibrium phase diagram. (after Hansen, Constitution of Binary Alloys, 2nd edition, McGraw-Hill, New York, USA, 1958).[18]*

The information that can be gathered from the phase diagram is plenty, but from heating and austenite point of view the information of interest are the temperatures critical to the austenitization process. The process starts at the A_1 temperature, where the eutectoid reaction occurs. In the equilibrium phase diagram this is at 723°C. A_3 is the temperature where the microstructure is full austenite, and in the diagram it is at 910°C for pure iron. [18] As can be seen from figure 3.9, the A_3 temperature is highly dependent on the carbon content, but also other alloying elements affect the value of A_1 and A_3. The equations for the transformation temperatures in a controlled heating process (A_{c1} and A_{c3}) are defined by Andrews [21] as follows:

$$A_{c3}(°C) = 910 - 203\sqrt{C} - 15.2Ni + 44.7Si + 104V + 31.5Mo + 13.1W \quad (3.15)$$

$$A_{c1}(°C) = 723 - 10.7\text{Mn} - 16.9Ni + 29.1Si + 16.9Cr + 290As + 6.38W \quad (3.16)$$

where the element symbols represent the content of the element in question. There are also some additional effects of more elements on A_{c3} in the original reference. [23]

It is worth mentioning, that the above mentioned equations are valid only for relatively slow heating processes and are not comparable for rapid heating processes, for example flame-cutting. The value of A_{c3} is highly sensitive to the heating rate with alloyed steels, which is demonstrated in a time-temperature-austenitization (TTA) diagram in figure 3.10 for Ck 45 steel (similar to AISI 1045). For pure iron the A_{c3} temperature varies much less according to the heating rate and the Andrews equation is more usable. [23]

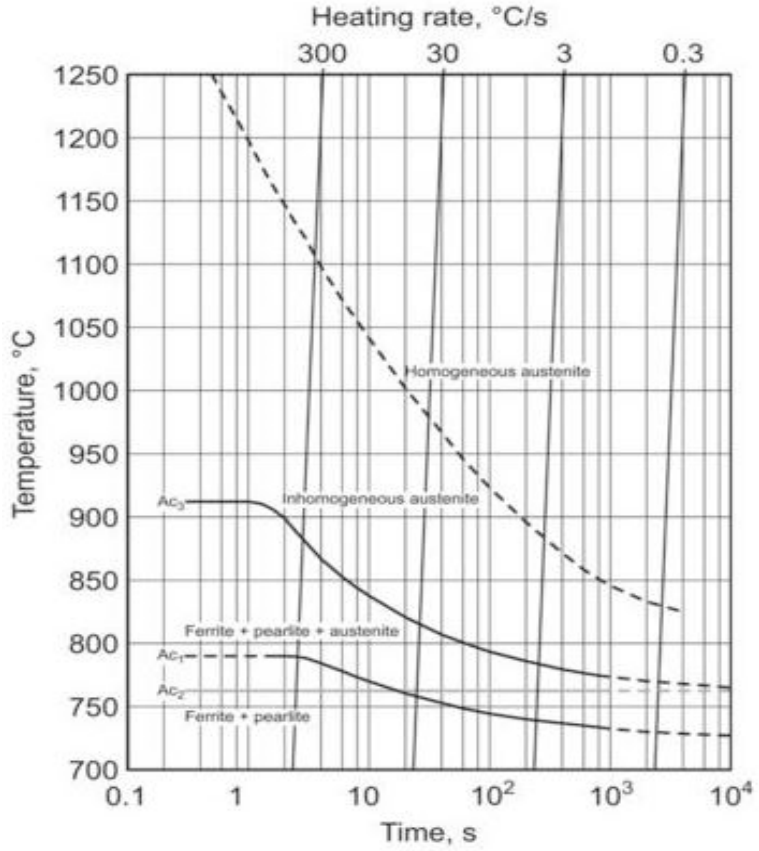

Figure 3.10. *Time-temperature-austenitization diagram for Ck 45 steel. [34] Reprinted from [23]*

The graphs shown in figure 3.10 are a result of nonequilibrium effects related to the behavior of carbides during austenitizing, which happen at high heating rates. After carbide dissolution at A_{c3} temperature, there might still be an inhomogeneous carbon distribution in the austenite until the carbon spreads evenly to create a homogeneous austenite. [23]

In conclusion, austenitization of steel in heating is extremely hard to predict due to the individual characteristics of alloyed steels and processes. Initial microstructure of steel and the heat treatment process have a major influence in the mechanisms by which austenite may form. Thus, alloyed steels are usually studied individually for more accurate results. [24]

3.2.2 Martensite

Martensite is a very hard metastable phase that is formed when an austenitized iron-carbon alloy is rapidly cooled so that carbon diffusion is not possible. Martensite is a nonequilibrium single-phase structure that is an outcome of a diffusionless transformation of austenite. Because martensite transformation is diffusionless, it does not appear on equilibrium phase diagrams, but the temperatures, at which martensite can form, can be presented in continuous cooling transformation (CCT) diagrams. [16, 17] The chemical composition for martensite is identified to be identical to the parent austenite, which further proves that the martensite transformation is diffusionless. [18]

Transformation of martensite is not thoroughly understood, but it is known that the mechanism behind the transformation is instantaneous shear displacement between the atoms and volume expansion. The displacement of one atom is smaller than the distance between the atoms. The transformation is a process where FCC austenite experiences a polymorphic transformation to a body-centered tetragonal (BCT) martensite, which is a body-centered cube that has been elongated along one of its dimensions, as presented in figure 3.8. The martensite reaction depends on the temperature: martensite begins to form at a martensite start (M_s) temperature, and the transformation is complete when a martensite finish (M_f) temperature is reached. The M_f temperature is often referred as the temperature where 95% of martensitic transformation is completed. The M_s and M_f temperatures are dependent on the composition of the steel. [16, 17, 18]

The martensite transformation happens athermally, which means that it does not require heat to occur. It is an extremely rapid time-independent process where martensite grains nucleate and grow. The progression of martensite transformation depends on the undercooling below the M_s temperature, as defined in the Koistinen and Marburger equation [18]

$$1 - V_{\alpha'} = \exp\{\beta(M_s - T_q)\} \tag{3.17}$$

where $V_{\alpha'}$ is the fraction of martensite and T_q the current temperature below M_s and β is a constant.

To create martensite, steel must be cooled down from austenitic phase with a rate that is rapid enough to avoid other solid-state phase transformations, such as bainite, ferrite or pearlite [18]. This is often achieved by quenching the steel. The cooling rate for producing an almost fully martensitic microstructure is called the critical cooling rate. This rate for different steels can be determined from the CCT-diagrams of those mentioned steels. This is important for heat treatment analysis, because hardening of the steel is often a desirable objective for heat treatment, and martensite is a hard phase. [19]

Chemical composition of the steel has a great impact on the characteristics of the martensitic transformation. M_s temperature is highly sensitive to the carbon content of the steel, as presented in figure 3.11.

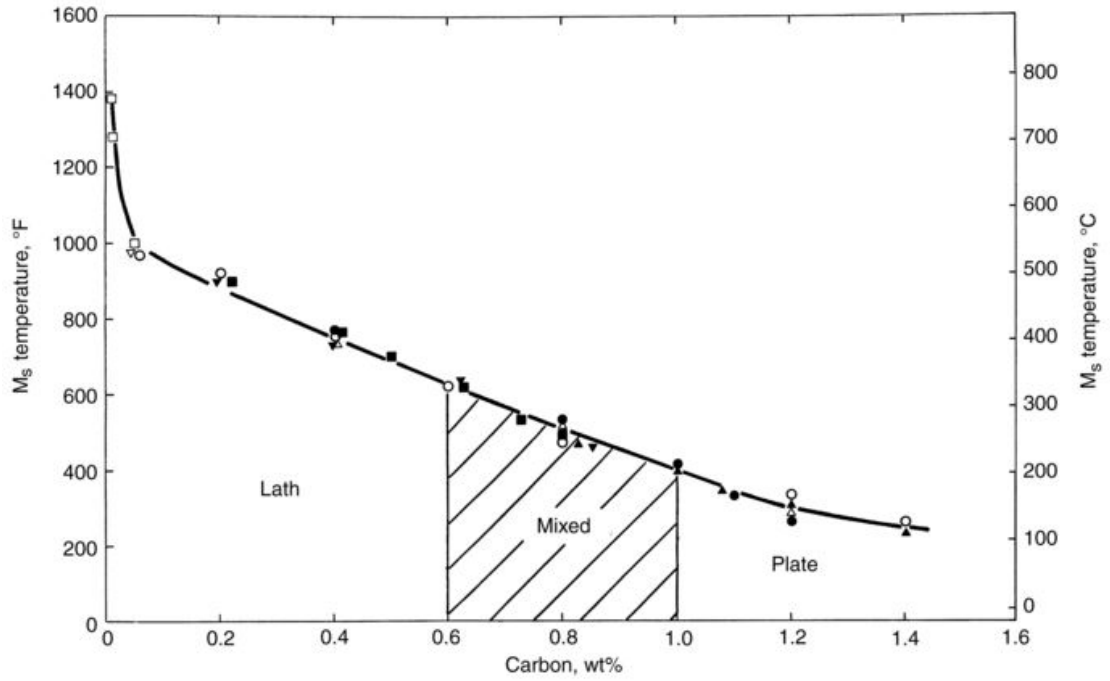

Figure 3.11. *Martensite start temperature values as a function of carbon content of the steel. [22]*

Although carbon is the most influential, it is not the only element that affects the martensitic reaction temperatures. Many alloying elements, such as nickel, chromium and molybdenum lower the M_s temperature. [17] Andrews [21] has created an equation that predicts the M_s temperature as a function of the element composition of the steel, stated as

$$M_s(°C) = 512 - 453C - 16.9Ni + 15Cr - 9.5Mo + 217(C)^2 - 71.5(C)(Mn) - 67.6(C)(Cr) \quad (3.18)$$

where the chemical symbols represent the content of the element in question.

3.3 Stress analysis

Stress analysis studies the cohesive forces between material particles, which hold the part together. In a continuum model, stress represents the mean values of the force effects between atoms from a macroscopic point of view. [25]

A part is at a state of rest, when the only internal forces are the ones keeping the part together, while no external forces are applied to the part, such as external point loads, gravitation or air pressure. Also internal forces induced by non-homogenous temperature field or manufacturing processes must be absent. Stress is a result of an event, where this natural state of equilibrium of the atoms is disturbed. However, a part can be at an external equilibrium, regardless of the residual stress field inside the part. [25]

Stress is defined as a force per unit area. Because stress is generally non-uniformly distributed throughout the part, infinitesimal elements are used for calculations. The elements are normally modeled as cubes, on whose faces the stress components apply on as shown in figure 3.12. The stresses acting perpendicular to the face of the element are called normal stresses, and the stresses acting parallel to the face are called shear stresses. [26]

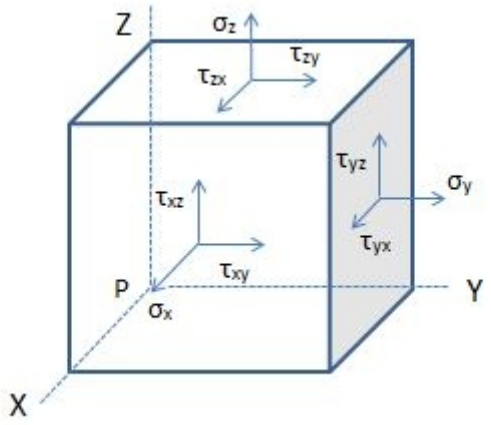

Figure 3.12. *Three-dimensional stress element of a point P. Reproduced from [25].*

The stress element in figure 3.12 can be presented as a stress matrix S,

$$[S] = \begin{bmatrix} \sigma_x & \tau_{xy} & \tau_{xz} \\ \tau_{xy} & \sigma_y & \tau_{yz} \\ \tau_{xz} & \tau_{yz} & \sigma_z \end{bmatrix} \tag{3.19}$$

where σ_i are the normal stresses and τ_{ii} are the shear stresses. Because the stress matrix is symmetric, shear stresses can be marked as equals by couple, which reduces the number of stress components for calculations. [25]

The axis system used in figure 3.12 is normally chosen for convenience reasons in computing. There is infinite number of shear planes, α, set for a specific point, P, and they create a group of tensors, $t_{\alpha i}$, which is called the state of stress of the point. The state of stress is a characteristic quantity for the point, and in engineering it is essential information for deformation and fracture analysis. All the states of stress of points form the stress state field of the part. [25]

To further discuss the analysis considering the state of stress, principal stresses must be taken into account. From the infinite number of shear planes, there are planes on which the shear-stress components are zero. Principal stresses are the normal stresses that are acting on these planes, and therefore they are the maximum values of normal stress affecting the point of interest. Similar to principal normal stresses, principal shear stresses are the maximum values of shear stress and act on the planes that are at 45° angles from the principal normal stress planes. [26]

The relation between the applied stresses and principal stresses can be expressed as

$$\begin{bmatrix} \sigma_x - \sigma & \tau_{xy} & \tau_{xz} \\ \tau_{xy} & \sigma_y - \sigma & \tau_{yz} \\ \tau_{xz} & \tau_{yz} & \sigma_z - \sigma \end{bmatrix} \begin{bmatrix} n_x \\ n_y \\ n_z \end{bmatrix} = \begin{bmatrix} 0 \\ 0 \\ 0 \end{bmatrix} \tag{3.20}$$

where σ is the principal stress magnitude and n_i are the direction cosines of the unit vector **n**, which is normal to the principal plane. [26]

The solution for equation 3.20 is that the determinant of the coefficient matrix is zero. This way we obtain a characteristic equation which can be solved. By marking

$$C_2 = \sigma_x + \sigma_y + \sigma_z \tag{3.21a}$$

$$C_1 = \tau^2_{xy} + \tau^2_{yz} + \tau^2_{zx} - \sigma_x\sigma_y - \sigma_y\sigma_z - \sigma_z\sigma_x \tag{3.21b}$$

$$C_0 = \sigma_x\sigma_y\sigma_z + 2\tau_{xy}\tau_{yz}\tau_{zx} - \sigma_x\tau^2_{yz} - \sigma_y\tau^2_{zx} - \sigma_z\tau^2_{xy} \tag{3.21c}$$

where C_i are called as the principal tensor invariants. The solution for equation 3.X can be written as

$$\sigma^3 - C_2\sigma^2 - C_1\sigma - C_0 = 0 \tag{3.22}$$

The roots of this polynomial are the principal normal stresses σ_1, σ_2 and σ_3. They are usually set in a decreasing order, as $\sigma_1 > \sigma_2 > \sigma_3$. The principal shear stresses can be calculated using the principal normal stresses as

$$\tau_{13} = \frac{|\sigma_1 - \sigma_3|}{2} \tag{3.23a}$$

$$\tau_{21} = \frac{|\sigma_2 - \sigma_1|}{2} \tag{3.23b}$$

$$\tau_{32} = \frac{|\sigma_3 - \sigma_2|}{2} \tag{3.23c}$$

If the principal normal stresses are set in a decreasing order, then the τ_{13} is the maximum value. [26]

In a principal coordinate system, where the shear-stress components are zero, the stress element is called the principal stress element, and it can be expressed as a diagonal matrix, whose diagonal elements are the principal normal stresses:

$$[S] = \begin{bmatrix} \sigma_1 & 0 & 0 \\ 0 & \sigma_2 & 0 \\ 0 & 0 & \sigma_3 \end{bmatrix} \tag{3.24}$$

By using the principal stress element, the stress analysis calculations simplify notably. For example, distortion energy yield theory states that the material yields at such a point, where the distortion energy density exceeds the yield strength of the ductile material. Using the distortion energy yield theory, an equation for Von Mises stress, σ_v, can be derived using the principal normal stresses as stated in equation X. Von Mises stress is commonly used in engineering as a criterion for material yielding.

$$\sigma_v = \left[\frac{(\sigma_1 - \sigma_2)^2 + (\sigma_2 - \sigma_3)^2 + (\sigma_1 - \sigma_3)^2}{2}\right]^{1/2} \tag{3.25}$$

The condition for the start of yielding can be compacted to

$$\sigma_v = \sigma_y \tag{3.26}$$

where σ_y is the yield strength of the material. [25]

3.3.1 Residual stress

Residual stresses are internal forces that act on an externally unloaded part. They are usually a result of the manufacturing processes done to the part, but any procedure that creates inhomogeneous plastic deformation leaves stresses to the part when the external loading is removed. These deformations can be divided to two groups:

- Volumetric strain, which is a result of thermal expansion, chemical conversion, microstructural transformation or change in state; [14]
- Distortional strain, which is a result of plastic deformation. [14]

Which strain is the source of the residual stress in the part is solely dependent on the process which was applied to the part. The objective in engineering considering residual stresses and the processes is to minimize the negative effects and create positive effects, if possible. [14, 26]

Fatigue and crack failure are stress-related phenomena that are highly receptive to the residual stress field of the part. It is commonly known that the mean compressive stresses have retarding effects on the crack progression and positive effects on the fatigue strength of the material. Thus, they are highly desired especially at the surface regions of the part to prevent any cracks to form or progress. Compressive residual stresses can be created to the part by many ways: by thermal treatments, surface treatments or mechanical stress treatments. [26] Thermal treatments will be further discussed due to the objectives of this thesis.

3.3.2 Residual stresses induced by flame-cutting

Case hardening as a thermal treatment process is equivalent to what happens to steel in flame-cutting: high density of heat is applied to the surface of the part for a small amount of time. The compressive residual stresses are created when the part is cooling down and volume increase by the phase transformation happens near the surface, and the core, where no transformations occur, pulls the surface into compression. Because the part is in equilibrium, the compressive stresses at the surface must be balanced as tensile stresses in the core. If the treatment process is not done correctly, these tensile stresses can cause failure in the material, therefore process optimization is required. [26]

To solve the temperature and stress gradients induced by flame-cutting, the process must be presented as a mathematical problem from a thermo-mechanical point of view. The thermal equation for temperatures can be expressed in tensor notation as

$$\rho c_p \dot{T} = (\lambda T_{,j})_{,j} + \dot{Q}_v \tag{3.27}$$

where ρ is the density, c_p is the specific heat, λ is the thermal conductivity, $T_{,j}$ is the temperature gradient and $\dot{Q}_v$ is the external heat applied to the part per unit volume. [7]

The mechanical problem can be presented in tensor notation by using the differential equations of force equilibrium:

$$\sigma_{ij,j} + p_i = 0 \tag{3.28}$$

where σ_{ij} is the stress tensor and p_i the body force at any point within the part. These body forces can be, for instance, gravity or heat radiation. [7]

As previously stated, residual stresses are a result of deformation, and the metric of deformation is strain. Thus, total strain of the material must be known to calculate the stresses inside the part. The total strain of a material that is experiencing phase transformations is often assumed [e.g., see ref. [7, 27-29]] to be a sum of different strains induced by various attributes. The equation for the total strain is:

$$d\varepsilon_{tot} = d\varepsilon_{el} + d\varepsilon_{th} + d\varepsilon_{tr} + d\varepsilon_{tp} + d\varepsilon_{pl} \tag{3.29}$$

$d\varepsilon_{el}$ is the elastic strain increment which is related to the stress rate by Hooke's law [see eq. Young modulus] . [29]

$d\varepsilon_{th}$ is the thermal strain increment that depends on the thermal expansion of the material. [29]

$d\varepsilon_{tr}$ is the strain increment related to the volume change due to the phase transformations of the material. [29]

$d\varepsilon_{tp}$ is the transformation plasticity strain increment. [29]

$d\varepsilon_{pl}$ is the plasticity strain increment, which takes into account all the inelastic behaviour of the material. [29]

According to Leblond et al. (1986), the equation can be simplified by including the transformation strains to $d\varepsilon_{th}$ for their isotropic part and to $d\varepsilon_{pl}$ for their deviatoric part [27, 28]. By doing this the equation 3.29 can be presented as:

$$d\varepsilon_{tot} = d\varepsilon_{el} + d\varepsilon_{th} + d\varepsilon_{pl} \tag{3.30}$$

To understand what kind of residual stresses are to be expected from the model in this thesis, some literature research is required. Lindgren et al. [6] studied the effects of flame-cutting in residual stresses by measurement and computing in two dimensions. A

model was created and then a 50mm thick plate was cut with a cutting speed of 4.83mm/s for verification. The computed and measured results are presented in figure 3.13 as an isoline stress field.

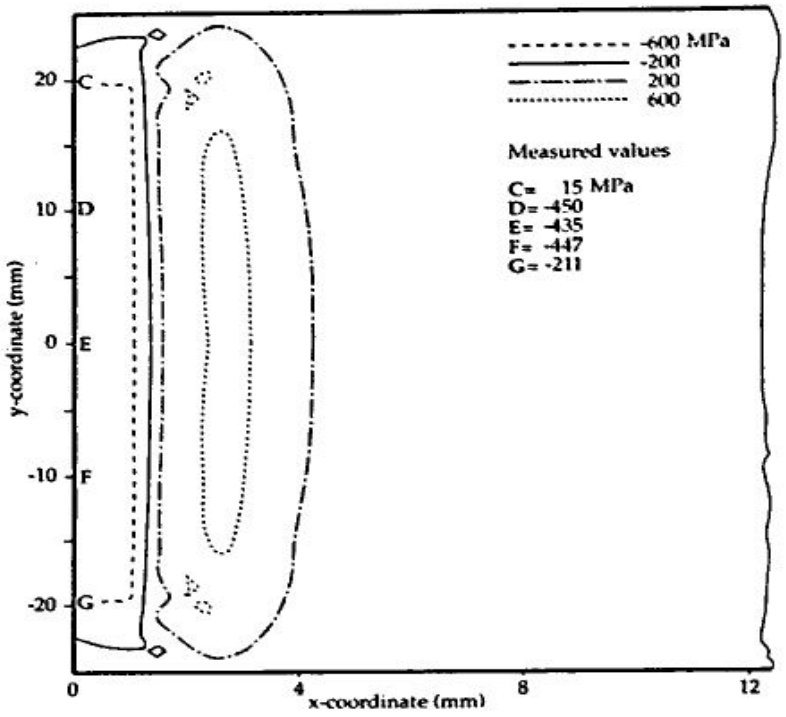

Figure 3.13. *Computed residual σ_{yy} isolines and measured values by Lindgren et al. [6]*

Lindgren et al. [6] also studied the effects of pre-heating in a flame-cut plate. The results from the calculations are shown in figure 3.14.

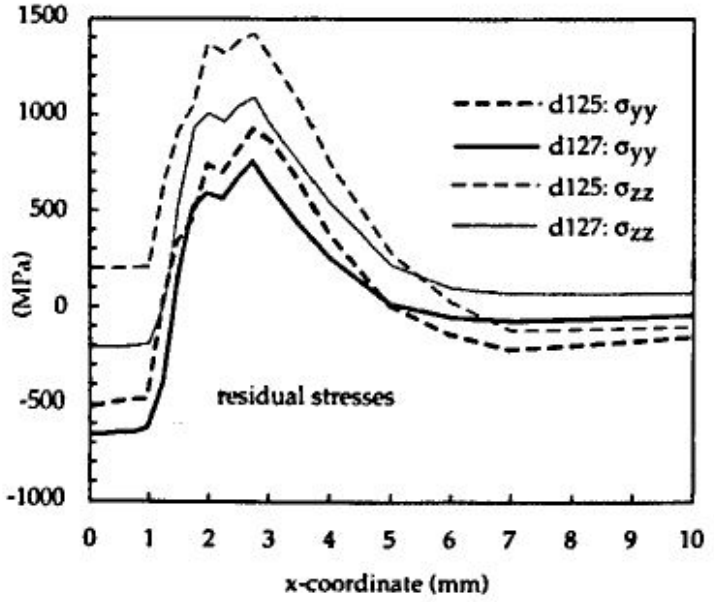

Figure 3.14. *Residual stresses in thickness direction and cutting direction by Lindgren et al., where y is the direction of thickness and z is the direction of the cut. Designation d127 represents the pre-heated plate and d125 the plate without pre-heating. [6]*

The results in figures 3.13 and 3.14 show that flame-cutting creates a compressive stress region at the surface of the cut, and high tensile stress is located in the core, as stated earlier. These results will be further discussed as a comparison between the computed results of this thesis.

3.3.3 Finite element approach on stresses

The calculation of heat induced stresses is extremely complicated due to the thermo-mechanically coupled nature of the process. Finite element method (FEM) is an analysis tool by which the computation can be successfully done. FEM is a method where a part is divided to a number of discrete elements, which are connected at their nodes, creating a mesh. Then the displacements and internal forces caused by the applied external loads and boundary conditions can be calculated by using the stiffness of the elements. [26]

To clarify the concept behind FEM, next is a simple example of displacement calculation of a beam that is restrained from the other and applied with a load at the other end. The calculation is done by using a three-node finite element mesh, shown in figure 3.15. [13, 26]

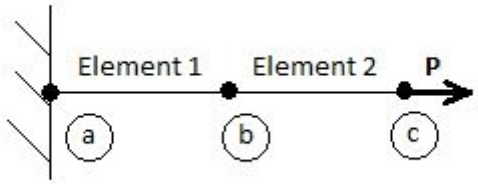

Figure 3.15. *Restrained beam applied with a load as a three-node finite element mesh.*

In figure 3.16 are the free-body diagrams of each node from figure 3.15. The forces acting on the nodes are from the applied external load, P, and the internal forces, I, which are the result of stresses acting in the elements fixed to the node in question. [13]

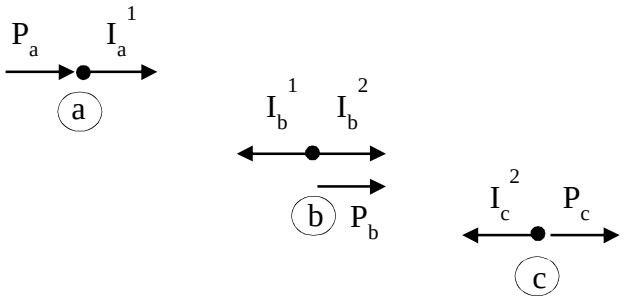

Figure 3.16. *Free-body diagrams of the nodes. [13]*

According to the equilibrium theorem stated above [see chapter 3.3], the internal and external forces acting on the node must balance each other out for the part to be in a state of rest. By using equations 3.5 (Hooke's law) and 3.9 (Engineering strain) the equilibrium equation for node a can be written as

$$P_a + \frac{EA}{L}(u_b - u_a) = 0 \tag{3.31}$$

where P_a is the external load in node a, E is the Young's modulus, A is the cross-section area of the beam, L is the original length of the element and u_i are the displacements of the nodes at issue. [13]

Then by creating the equations for each node and replacing the stiffness factors, EA/L, of the elements 1 and 2, with variables K_1 and K_2, an equilibrium matrix equation for the beam can be created:

$$\begin{Bmatrix} P_a \\ P_b \\ P_c \end{Bmatrix} - \begin{bmatrix} K_1 & -K_1 & 0 \\ -K_1 & (K_1 + K_2) & -K_2 \\ 0 & -K_2 & K_2 \end{bmatrix} \begin{Bmatrix} u_a \\ u_b \\ u_c \end{Bmatrix} = 0 \tag{3.32a}$$

or in matrix form:

$$[K]\{u\} = \{P\} \tag{3.32b}$$

The solution of the problem would then be obtained by inverting the stiffness matrix, [K], and solving the displacements, {u}.

To model and analyze flame-cutting of large steel plates in two dimensions with ABAQUS, proper analysis methods must be selected. Plane strain theory is a suitable method for thermal-stress analysis of thick bodies, such as a steel plate. In the theory, the strain tensor for the section is written as:

$$[V] = \begin{bmatrix} \varepsilon_{11} & \varepsilon_{12} & 0 \\ \varepsilon_{21} & \varepsilon_{22} & 0 \\ 0 & 0 & 0 \end{bmatrix} \tag{3.33}$$

where the strains in the third direction, in this case the z-direction, are assumed to be zero. The stress tensor for plane strain theory is written as:

$$[S] = \begin{bmatrix} \sigma_{11} & \sigma_{12} & 0 \\ \sigma_{21} & \sigma_{22} & 0 \\ 0 & 0 & \sigma_{33} \end{bmatrix} \tag{3.34}$$

where the normal stress in z-direction, σ_{33}, is needed to maintain constant $\varepsilon_{33} = 0$. The problem can be presented in equation form as

$$\varepsilon_{33}{}^{tot} = \frac{\sigma_{33} - \nu(\sigma_{11} + \sigma_{22})}{E} + \varepsilon_{33}{}^{pl} = 0 \tag{3.35}$$

By using the plane strain theory, a two-dimensional part can be modeled with the stresses and strains in the third direction taken into consideration. The total strain in the third direction is zero, when the poisson effect and the plastic strain is counteracted by the normal stress in the same direction. The values of these strains and stresses can be obtained from the calculation.

For a problem where the mechanical and the thermal behavior are strongly connected, such as flame-cutting, ABAQUS uses a fully coupled thermal stress analysis. This means that the stress and temperature distributions are interdependent, and therefore are calculated accordingly. In ABAQUS/Standard the nonlinear coupled system is solved using Newton's method involving a Jacobian matrix to create coupled equations stated as

$$\begin{bmatrix} K_{uu} & K_{u\theta} \\ K_{\theta u} & K_{\theta\theta} \end{bmatrix} \begin{Bmatrix} \Delta u \\ \Delta\theta \end{Bmatrix} = \begin{Bmatrix} R_u \\ R_\theta \end{Bmatrix}, \tag{3.36}$$

where K_{ij} are the submatrices of the fully coupled Jacobian matrix, R_i are the mechanical and thermal residual vectors and Δu and $\Delta\theta$ are the corrections to the incremental displacement and temperature, respectively. [13]

The physical behavior of the material can be more accurately simulated by using the fully coupled thermal stress analysis, which leads to more reliable results. With the plane strain theory combined to the analysis, an assumption can be made that the simulation of flame-cutting process as a two-dimensional model should produce sufficiently accurate results with reasonable computing costs.

4. THERMOMECHANICAL ANALYSIS

4.1 Modelling of flame-cut steel plate

Modelling the part for thermal cutting is straightforward, due to the rectangular shape of the steel plate. Therefore the main attention was focused on creating the finite element mesh and boundary conditions for the part. The part was set to a thickness (y-direction) of 40 millimeters and the width (x-direction) was chosen, so that the part could be assumed as infinite.

4.1.1 Meshing the part

The size and density of the finite element mesh has a major effect on the accuracy of the results and computational time of the simulation [15]. Two meshes were created so that there was no need to optimize between the two above-mentioned variables; a dense mesh with over 33 000 elements, which is presented in figure 4.1, and a coarse one with a little over 5000 elements. With two meshes, iterative calculations could be conducted rapidly with the coarse mesh, and after a series of iterations to ensure the model worked properly, accurate results could be obtained with the dense mesh.

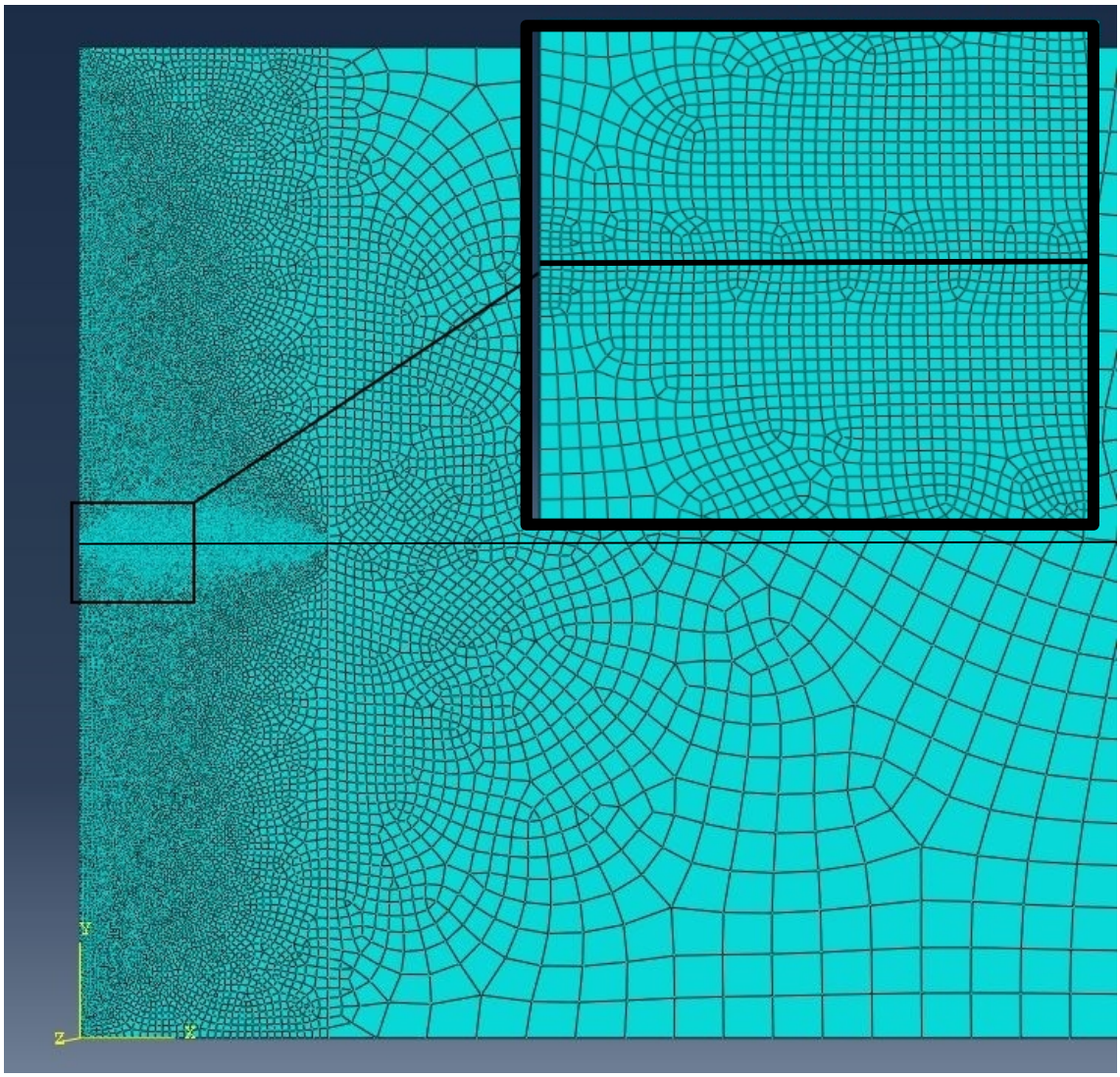

Figure 4.1. *Finite element mesh with 33294 elements with a zoom from the middle line.*

4-node plane strain thermally coupled quadrilateral, bilinear displacement and temperature elements were chosen for the mesh from standard element library. Quad-dominated element shape was chosen to prevent any distortion from happening. To ensure accurate results from the area of interest, thicker mesh was created to the middle section of the part, as can be seen from figure 4.1. The element size in this area was set to $4x10^{-5}$ m. The straight line in x-direction in figure 4.1 is the middle line, which will be used as the inspection line for the results in chapter 5.

After the part was created and meshed, some boundary conditions were applied to it. For the thermal boundary conditions, convective heat transfer coefficient was set to 8 $W/(m^2K)$ and for radiation heat loss the emissivity was set to 0.2 and Boltzmann constant was set to 1.38065×10^{-23} m^2kg/s^2K. These boundary conditions were also applied to the cut edge on the second step after the cut was done. As mechanical boundary conditions, the part was fixed from the far bottom corner to prevent any movement in x-direction, and supported (fixed) from the bottom in y-direction.

4.1.2 Modelling of low-alloyed steel

To make a model, in which the chosen material behaves like the equivalent one in the real world, is a difficult task. There are plenty of references for material properties of steel in the literature, but the difficulty lies in finding the right reference with the right alloys. As mentioned above, the behavior of steel is largely dependent on the composition; therefore the importance of finding material properties that are feasible is significant. Most of the material properties used in the model were created with JMatPro using the composition of the surveyed steel [see table 1], and the temperature history of the part obtained from initial FEM analyses.

It is worth noting, that the material property curves presented in figures 3.1-3.5 are used throughout the analysis. These curves present one particular temperature history in which the material heats up to fully austenitic state and cools down to room temperature. In the real part each material point has its individual temperature history, which affects the material properties (for example, material properties during cooling depend on the maximum temperature attained during heating). In principle, this should be taken into account in the simulations. However, this would notably add the complexity of the model and increase the amount of needed material data. Therefore, within the scope of this work, the simplified approach used here is considered justified.

When using JMatPro, the phase distribution of the part was also a subject of interest, in addition to the material properties. A CCT-diagram could be created for the surveyed steel, and by studying it together with a micrograph obtained with a scanning electron microscope (SEM), provided by the Technical University of Tampere, a prediction could be made that the heat affected part of the steel plate consists mainly/only of martensite. The CCT-diagram with a graph illustrating the cooling rate of the surveyed steel is presented in figure 4.2. The cooling rate was created from the temperature history output of ABAQUS.

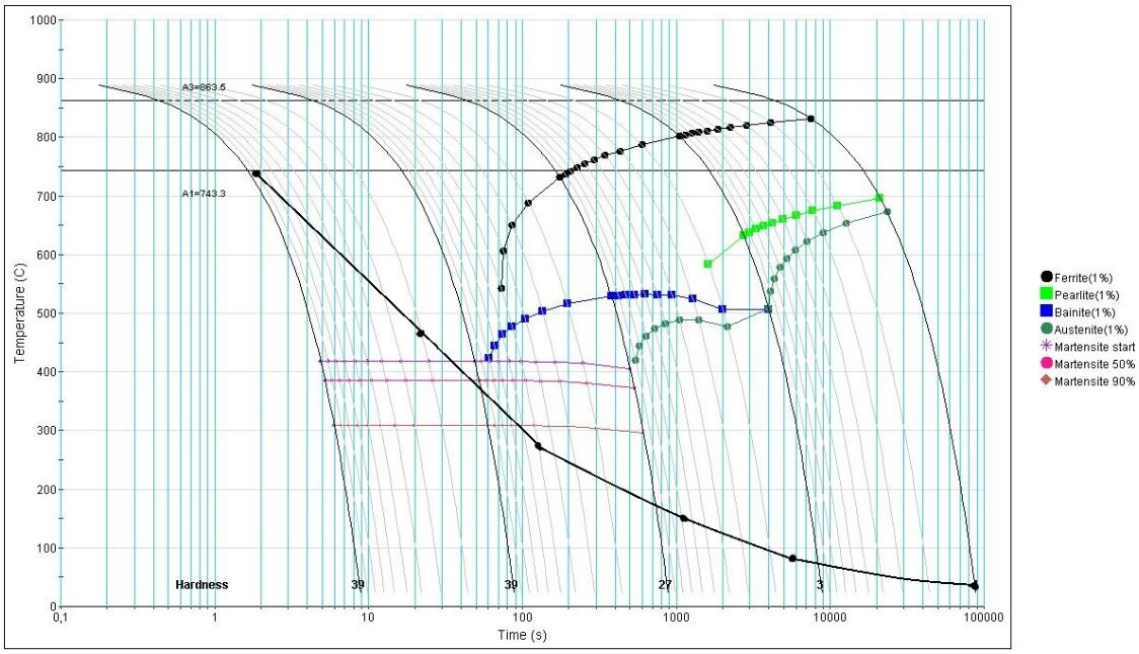

Figure 4.2. The *continuous cooling transformation (CCT) diagram and the cooling rate graph of the surveyed steel obtained from JMatPro and ABAQUS, respectively.*

As can been seen from figure 4.2, the bainite nose is avoided when the cooling rate is over 10°C/s. However, the graph is only a prediction and thus the actual steel plate can contain other phases than martensite, but in this thesis an assumption is made, that only phases of steel that exist during the whole thermal process are austenite and martensite. This way the user subroutines can be focused to a more specific task.

The phase transformation temperatures were calculated using different references. For the austenite start temperature, A_1, a value of 745°C was obtained using the Andrews equation [eq. 3.16]. As for the full austenite temperature, A_3, a different approach was needed, because of the rapid heat increase associated with flame-cutting affects the value of A_3 greatly, and therefore the Andrews equation may not apply. This is not the case with A_1, as it is assumed to be constant after [31]. Macedo et al. [31] have studied the effects of high heating rates on the value of A_3 as a function of austenite formation time, which is presented in figure 4.3.

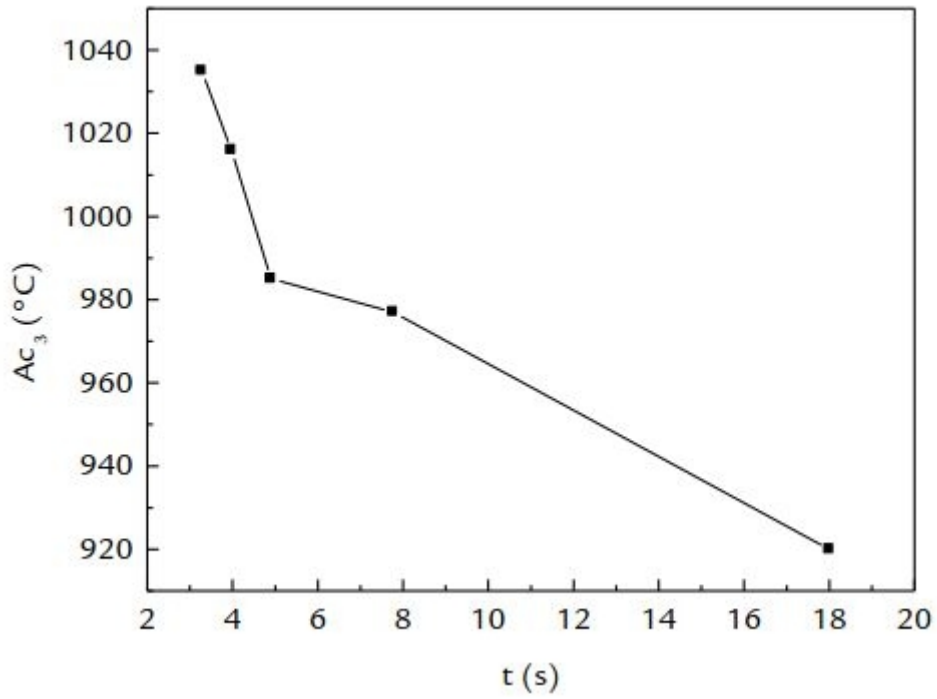

Figure 4.3. *The A_3 values as a function of the austenite transformation period for the SAE4130 steel. [31]*

Using the information from figure 4.3, a conclusion can be drawn that as the time of the diffusion process decreases, the process requires more energy to happen, which is provided at a higher temperature. Therefore a greater A_3 value is needed. In this thesis the value was chosen after comparing the temperature distribution from the model with the SEM micrograph, and was accordingly set to 1077°C. The phase transformation temperatures used in creating the model are presented in table 2.

Table 2. *Values of the used phase transformation temperatures.*

Temperature	Value [°C]	Value [K]
A_3	1077	1350
A_1	745	1018
M_s	440	713
M_f	234	507

The values for martensite phase transformation temperatures were calculated using modified equations from Andrews [21]. There can be slight inaccuracies in the temperature values in table 2, as the heating rates fluctuate during the cut process, and the equations do not take all the alloyed elements into consideration. Also the interpretation of the SEM photo is somewhat subjective; therefore a margin of error is always present.

4.1.3 User subroutines

In this chapter the subroutines used for the simulation are presented. Subroutines are essential for the calculations, because with them the finite elements can be assigned to act differently according to their temperature history. This way the material is not totally homogeneous, and the phases, in this case martensite and austenite, can be implemented into the model. The effect of phase transformations were included to the thermal expansion coefficient, α, and the material properties of the steel were set to vary whether the part was heating up or cooling down [see fig. 3.1-3.7].

First the user subroutine USDFLD (USER DEFINED FIELD) was used to define field variables for the material properties. The field variable, FIELD(1), obtains a value of 1 or 2, whether the temperature change between increments was positive or negative. The value of the field variable determines which values of the material properties the program uses for the calculation.

Next step was using a utility routine GETVRM, which accesses material point data and provides the temperature information at each increment. By using this information, state variables, STATEV(X), could be determined by the maximum temperature of each material point. The elements were marked with a value from 0 to 3, which indicated the temperature range in which their maximum temperature settled. The limits for the values were chosen as the phase transformation temperatures A_1, A_3 and melting point. If the material point never reached the A_1 temperature, it was given a value of zero. If the maximum temperature of the material point was in the two-phase region between A_1 and A_3, the value was set to one. Value of two was given to the elements between full austenite, A_3, and melting point, and value of three was given to liquid steel. These values indicated the phase distribution of the part [see fig. 5.4], and was later used as boundary values for the thermal expansion coefficient.

As stated earlier, the volume expansions of the phase transformations were included to the thermal expansion coefficient for computing reasons. This was done by using a subroutine called UEXPAN, in which the user can define the thermal expansion of the finite elements by the temperature change of the increment. Phase transformation temperatures were used as boundaries for the changes in the thermal expansion coefficient and

the phase fractions were defined as follows: the martensite fraction, f_m, was calculated by using the equation 3.17 as

$$f_m = 1 - \exp\{\beta(M_s - T)\} \tag{4.1}$$

where β is -0.04 and M_s is 713K.

The graph of martensite fraction using equation 4.1 is presented in figure 4.4. The constant β was selected so that the 50 percent of the martensite transformation happens almost instantly, which is generally assumed.

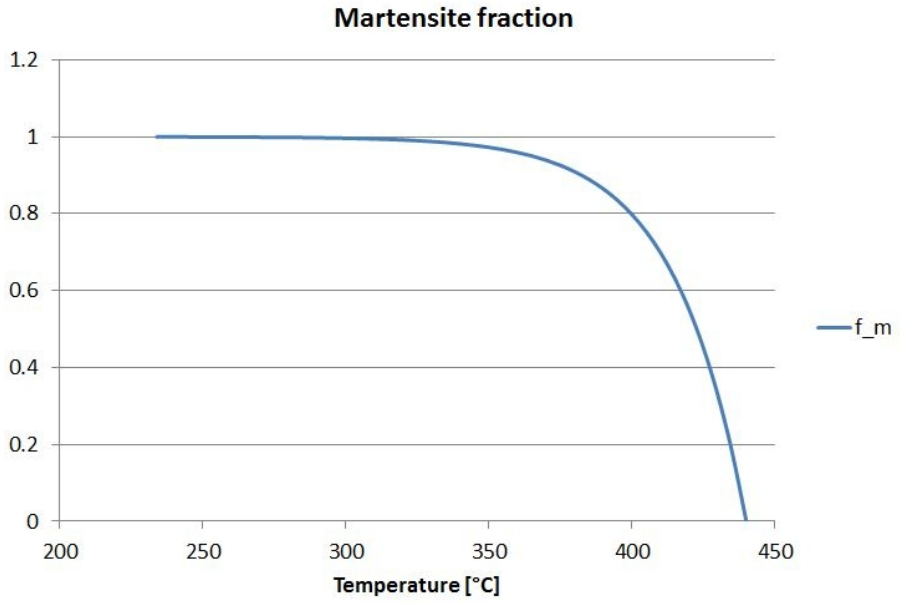

Figure 4.4. *Graph of the fraction of martensite by using the modified Koistinen-Marburger equation 4.1.*

For austenite, the phase fraction, f_a, was calculated using a modified Avrami-function called Weibull's cumulative distribution function [30]:

$$f_a = f_{a_{final}}(1 - \exp\{A(\frac{T - A_1}{A_3 - A_1})^B\} \tag{4.2}$$

where f_{a_final} is the phase fraction at the end of the transformation, A and B are material dependent constants, set to -6 and 2 respectively. The graph for the austenite fraction is presented in figure 4.5.

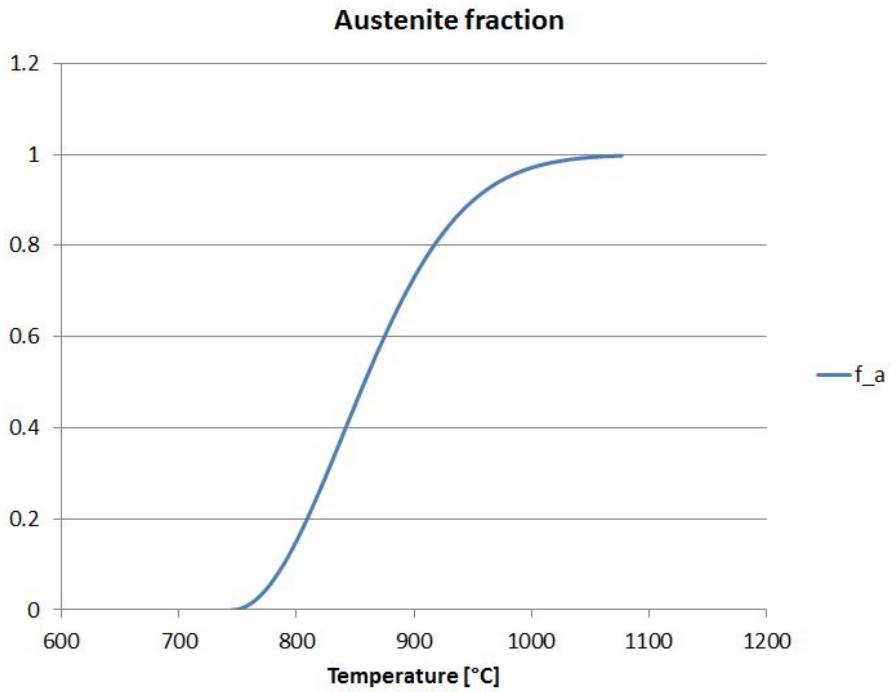

Figure 4.5. *Graph of the fraction of austenite by using the Weibull's cumulative distribution function.*

By using the state variables as boundary values, the thermal expansion coefficient could be determined for the elements that reach the phase transformation temperatures. For the elements that did not reach the A_1 temperature, the thermal expansion coefficient was set to the value of parent steel, $\alpha_s = 13 * 10^{-6}$ 1/K. The same value was used for the thermal expansion coefficient of martensite, α_m. When the part was heating up, the effect of austenite formation in the thermal axial expansion, $\Delta L/L$, was taken into account by combining α_s and the expansion coefficient of austenite, α_a (= $20 * 10^{-6}$ 1/K), with the austenite phase fraction as:

$$\frac{\Delta L}{L} = (f_a \alpha_a + (1 - f_a)\alpha_s)\Delta T \tag{4.3}$$

where ΔT is the temperature change of the increment.

The total volume expansion of martensite, $\Delta V_m/V_m$, was defined by comparing the computed results with the measured results by [33], and was set to an axial deformation, $\Delta x_m/x_m$, of 0.75 percent, which translates approximately into a volume expansion of 2.3 percent. The effect of the volume expansion is further discussed in the results. The thermal axial expansion, which included the volume expansion of martensite transformation, for elements that partially or fully transformed into austenite, and cooled down to the range of martensite transformation temperatures, M_s and M_f, was calculated as follows:

$$\frac{\Delta L}{L} = \{f_a((1-f_m)\alpha_a + (f_m\alpha_m) + \left(\frac{\frac{\Delta x_m}{x_m}}{M_f - M_S}\right)) + (1-f_a)\alpha_s\}\Delta T \qquad (4.4)$$

By doing this, the strain from the martensitic phase transformation is fully included to the thermal strain increment, without the deviatoric part, which is used in the calculation of the total strain [see eq. 3.30]. In the subroutine, the thermal expansion is assumed to be isotropic, therefore the volume expansion of the elements, ΔV/V, can be derived using the thermal axial expansion as:

$$\frac{\Delta V}{V} = \left(1 + \frac{\Delta L}{L}\right)^3 - 1 \qquad (4.5)$$

The use of subroutines in the model was immensely advantageous, and further study could improve the results of the model. For example, the code does not take annealing of the parent steel into consideration, though it is known to have significant impact on the stress distribution inside the steel plate. Also other phase transformations, such as bainite or ferrite, could be implemented to the subroutine. This way the model would be much more flexible and have a variety of utilization possibilities.

4.2 Flame modelling

To simulate the process of flame-cutting of a steel plate, one of the most significant aspects is the modelling of the flame and the effects it has on the applied surface. Because of the objectives of this thesis, an actual cutting simulation is not warranted, thus making the removal of elements unnecessary. For thermal analysis, the melting of elements is taken into consideration via some changes in the material properties. For mechanical analysis, the elements will not reach the melting temperature; therefore no real cutting will occur. This was done for convenience reasons, so that the “molten” elements will not disturb the stress analysis near the surface, as they are not removed or altered.

From thermal simulation point of view, flame-cutting is an extremely complex process with a large set of variables, which are difficult to verify. In figure 4.6 is an energy flow chart of flame-cutting, which illustrates the factors affecting the net heat that is transferred to the solid material. The object of this thesis is not in creating a perfect model of the cutting flame; instead it is in finding out what happens inside the steel plate when it is subjected with a large amount of heat. This is why some simplifications will be made in the modelling of the flame.

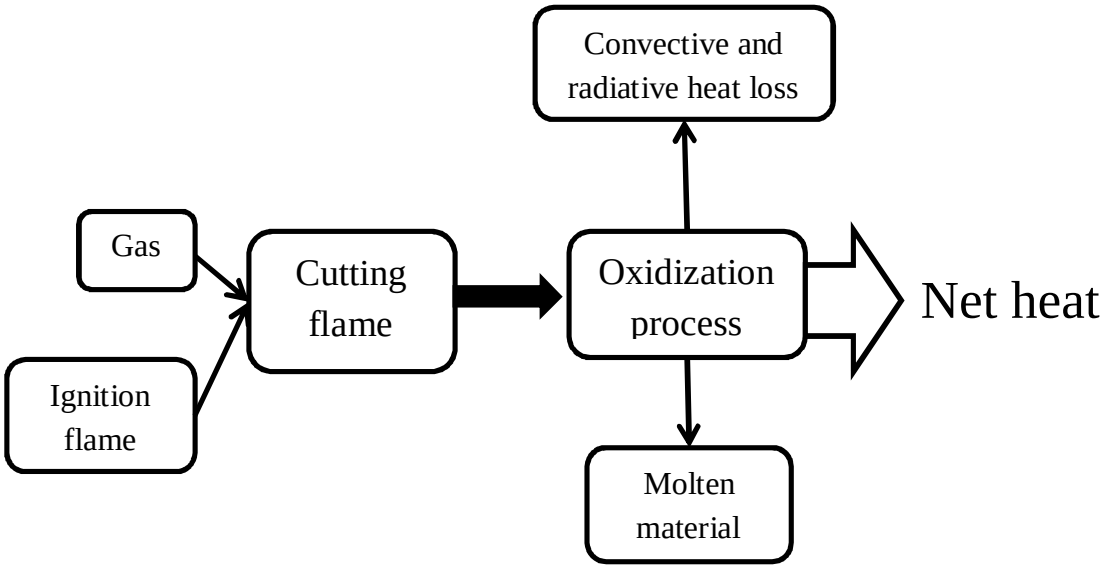

Figure 4.6. *Energy flow chart of the flame cutting process.*

When modelling the flame for thermal cutting in ABAQUS, it must be implemented as a heat energy flux. In three-dimensional environment the heat generated by the flame is often modelled in a cylindrical form moving along the cutting direction as in reference [5]. For two-dimensional simulation the flame must be simplified to a surface heat flux that is distributed along the cut edge as shown in figure 4.6. This method is sufficient to simulate the actual thermal cutting process from a heat distribution point of view, and it was used by Lindgren et al. [6,32]

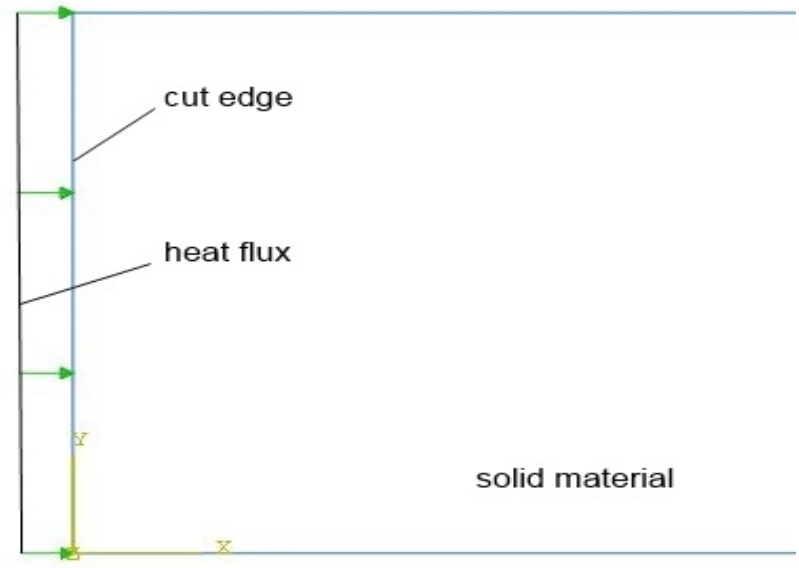

Figure 4.7. *Distribution of heat along the cut edge where Y-axis is the cutting depth.*

The heat flux presented in figure 4.7 is not totally uniform. Upper side of the cut receives more heat because of the flame has a higher impact there. This is complementary with the fact that the upper side of the cut has a bigger HAZ compared to middle section, which is demonstrated by Thiébaud et al. [5]

To create a flame that is moving along the Z-axis in two dimensions, ABAQUS has a feature that allows user to change the amplitude of the heat flux magnitude according to specific time. This feature was optimized for 150mm/min cutting using a simple three-dimensional model with a moving heat source as presented in figure 4.8. Nodes were selected from the center of the surface, and the temperature histories of those nodes were studied to determine how long the heat flux has effect on a single node.

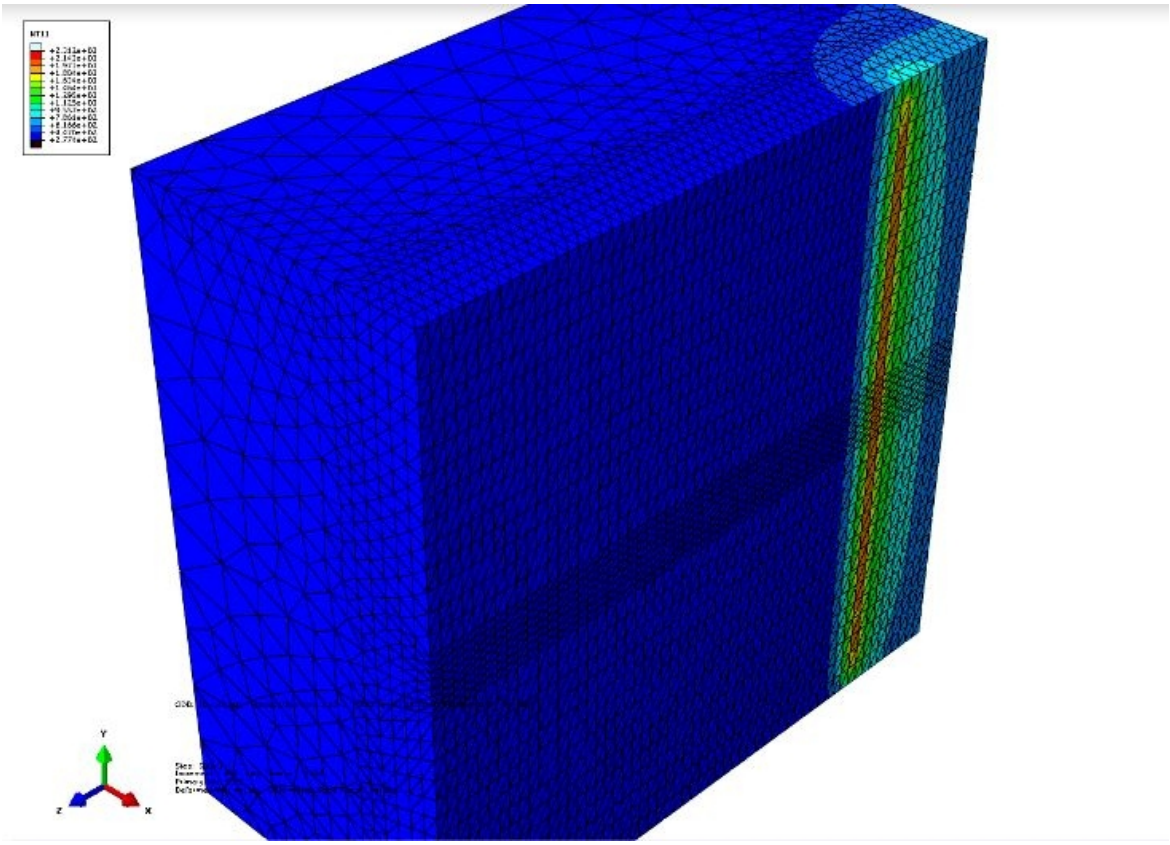

Figure 4.8. *Three-dimensional simulation used to help optimize the amplitude distribution of the heat flux for the two-dimensional model.*

With the data achieved from the three-dimensional simulation and temperature measurements made by the customer, an amplitude distribution graph for the heat flux could be created. This graph is presented in figure 4.9 and it was utilized to create distribution graphs for other cutting speeds, such as 300mm/min, 500mm/min and even 1000mm/min.

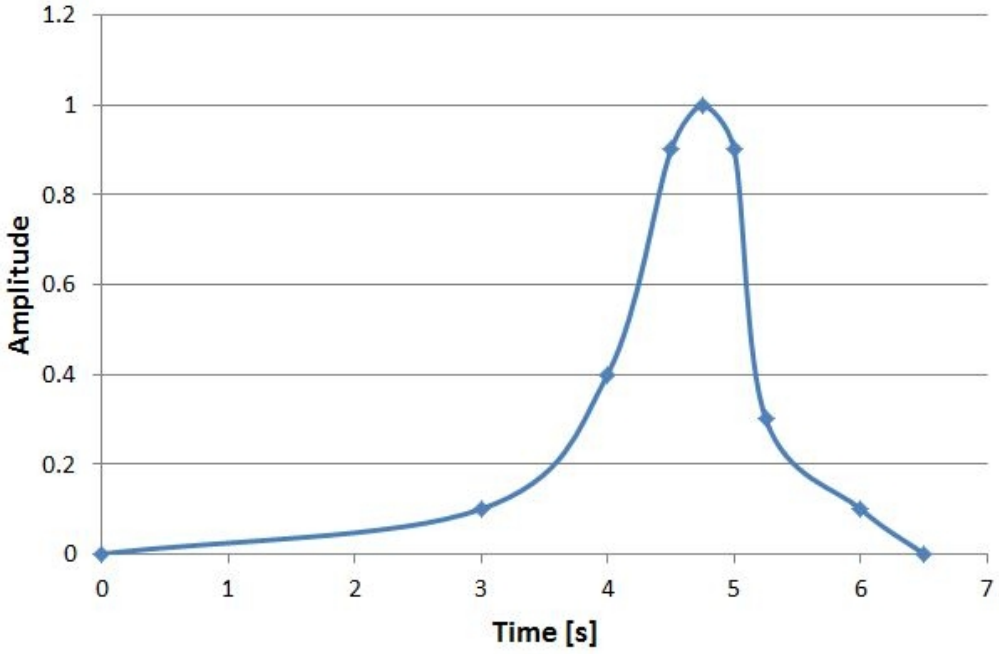

Figure 4.9. *Heat flux amplitude distribution for cutting speed of 150mm/min.*

The time frame between 4.5 and 5 seconds simulates the moment when the flame hits the cut edge. The time frame between 0 and 4.5 seconds simulates heat transfer that happens through conduction before the flame arrives. After the flame has passed, it still transfers heat to a specific point and that is presented between 5 and 6.5 seconds. For the other cutting speeds, the time frames were divided accordingly how quick the process is compared to 150mm/min cutting.

Heat input was selected by iterating the correct magnitude for the heat flux. For thermal analysis different magnitudes were tested until the surface elements in the middle section reached temperature above the melting point of 1520 °C. For stress analysis the heat flux magnitude was chosen so that the maximum temperature of the surface elements reaches values just below the melting point. This was imperative so that there was no need to remove elements or set them to zero, which would have undesired effect on the analysis of the stress curves at the surface region. The selected heat input for 150 mm/min cutting was 1.65×10^7 W/m^2 for stress and 1.8×10^7 W/m^2 for thermal analysis. This is comparable with the one used by Lindgren et al, considering that the heat distribution is time-dependent and not uniform. Heat losses of the flame can be in this case ignored, since the heat flux directed to the part is already the net heat.

5. RESULTS AND DISCUSSION

The outcomes of the FEM simulations are presented in this chapter. The temperature results played a significant role in the improvement of the model, as much of the material behavior analysis was based on the temperature data provided by the calculations. All of the calculations were made with a 40mm thick steel plate, with the exception of the study on flame-cutting with different thicknesses, where 20mm and 60mm thick plates were also used. In the result figures, x-axis title Distance is the distance along the middle line from the cut edge.

5.1 Temperature

First results from the model were temperature related, since the creation of the model was iterative, and the phase analysis depended on the heating and cooling rates of the part. By obtaining the temperature history of the part, some validation for the flame model could also be made by comparing the graphs with the measurements provided by the customer. Figures 5.1 and 5.2 show the temperature curves of different distances from the cut edge calculated with cutting speeds of 300mm/min and 150mm/min respectively. The nodes were selected from the middle line since the mesh is finer there, which means that the results are more accurate.

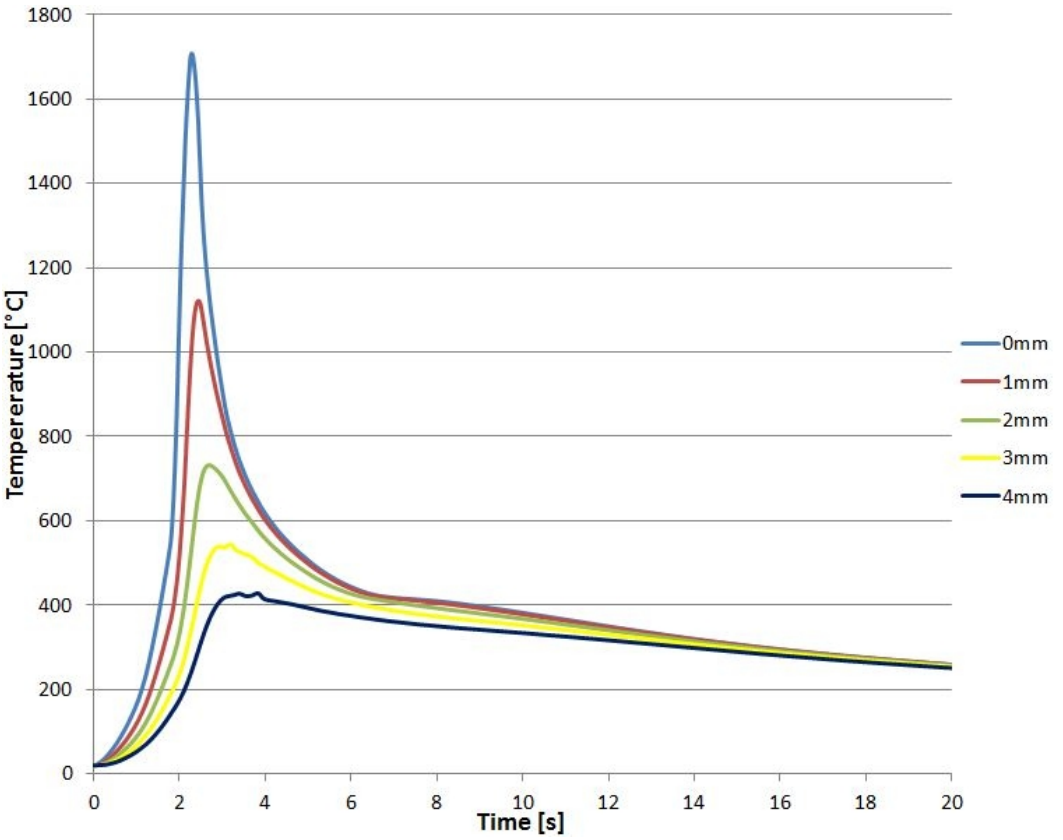

Figure 5.1. *Temperature at different distances from the cut edge during 300mm/min flame-cutting.*

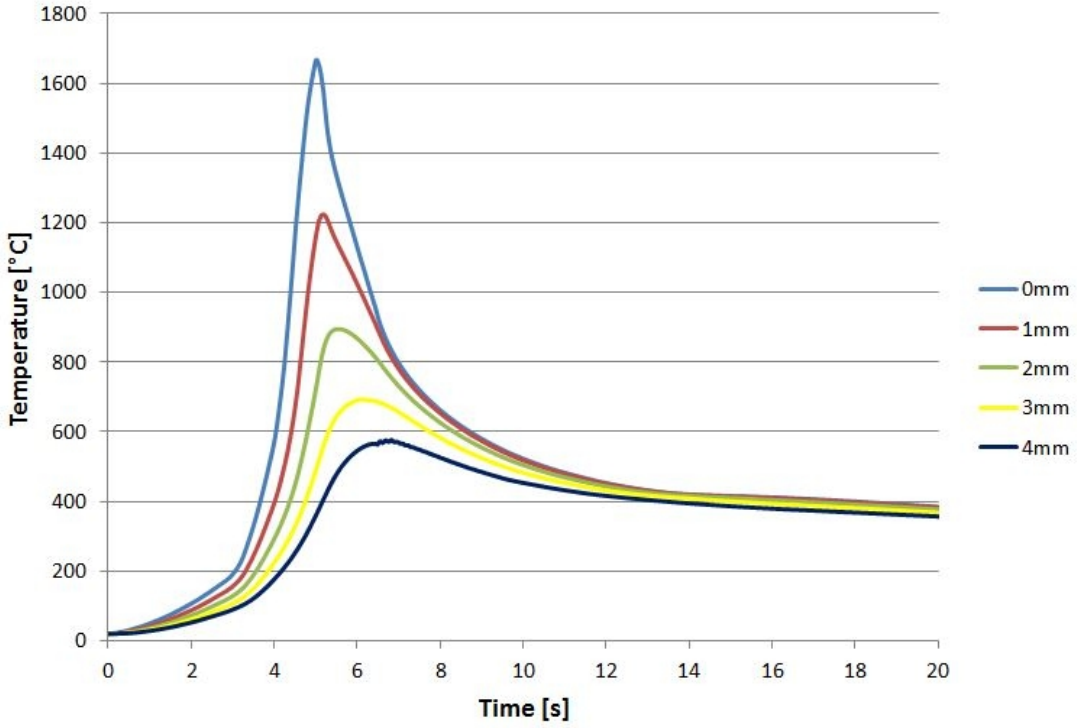

Figure 5.2. *Temperature of different distances from the cut edge during 150mm/min flame-cutting.*

The heating and cooling rates can be calculated from the information provided by the graphs in figures 5.1 and 5.2. The heating rate exceeded the value of 2000°C/s at some points, therefore the used A_3 temperature was well justified. The cooling rate of the part, which was used in the determination of the phases included in this study, can be seen from figure 4.2 with the CCT diagram. The cooling rate was calculated from a distance of 2mm from the cut edge, to ensure that all the elements experiencing phase transformations would avoid the bainite nose.

Maximum temperatures, T_{max}, of the nodes were used as a state variable for the user subroutines. T_{max} were used to calculate the austenite fraction [see eq. 4.2] of the elements, which was later utilized in the calculation of the total axial expansion [see eq. 4.4]. The maximum temperatures from the middle line are presented in figure 5.3.

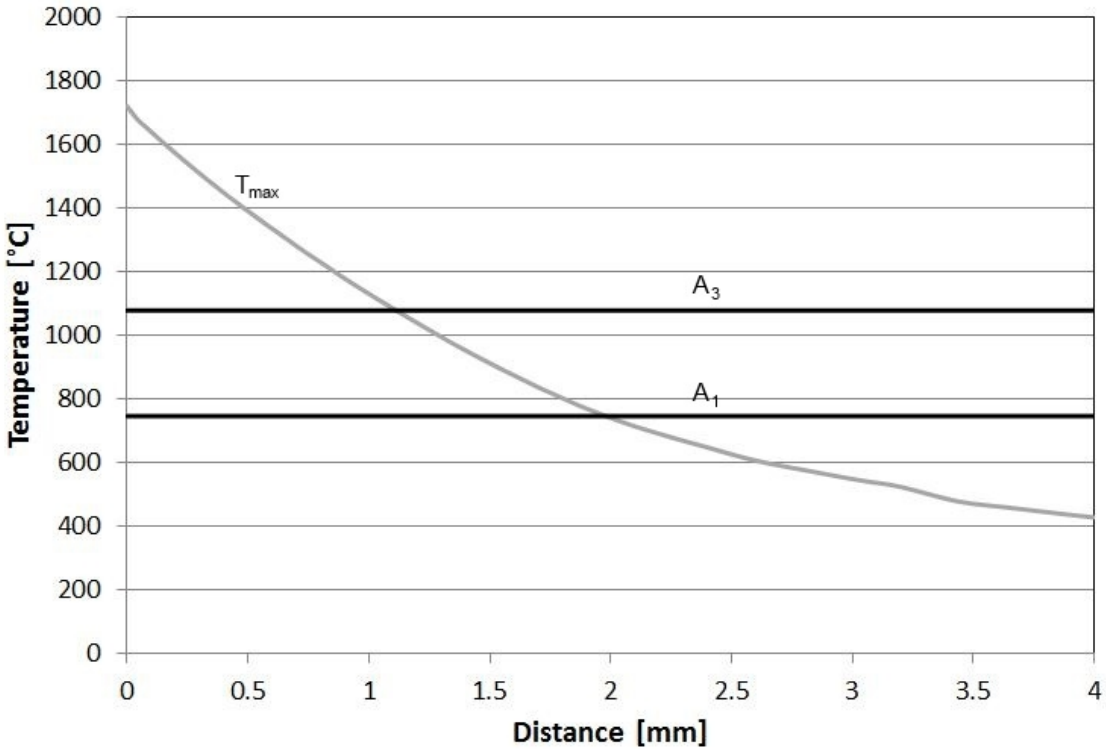

Figure 5.3. *Maximum temperatures of 300mm/min flame-cutting as a function of distance with austenite phase transformation temperature lines added.*

As a further explanation of figure 5.3, a phase region image from ABAQUS is presented in figure 5.4. The elements whose maximum temperature reach the specific phase transformation temperatures are colored according to the state variable mentioned in subsection 4.1.3. These are the regions that experience both austenite and martensite transformation and therefore are the elements of interest.

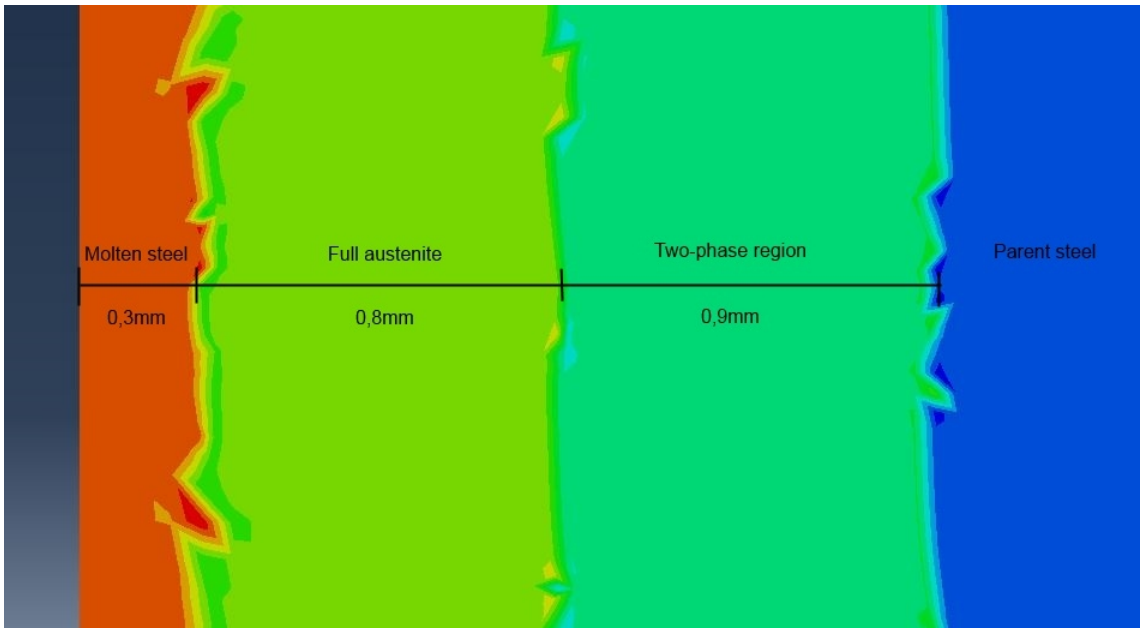

Figure 5.4. *Phase regions of 300mm/min flame-cutting for thermal analysis.*

The elements, which reached the melting point, were zeroed by changing their material properties similar to air. This way the heat from the flame went through the surface elements into the body without any significant heat loss. From a mechanical analysis perspective, these nullified elements disturbed the stress calculation of the part, and made the result analysis more difficult. Therefore, a second approach was made and the heat flux was adjusted so that the surface elements did not exceed the melting point. This way the surface elements are equivalent to the ones behind the molten steel region in figure 5.4. The phase transformation regions to the new approach are presented in figure 5.5. These regions will be used in the stress analysis of the part.

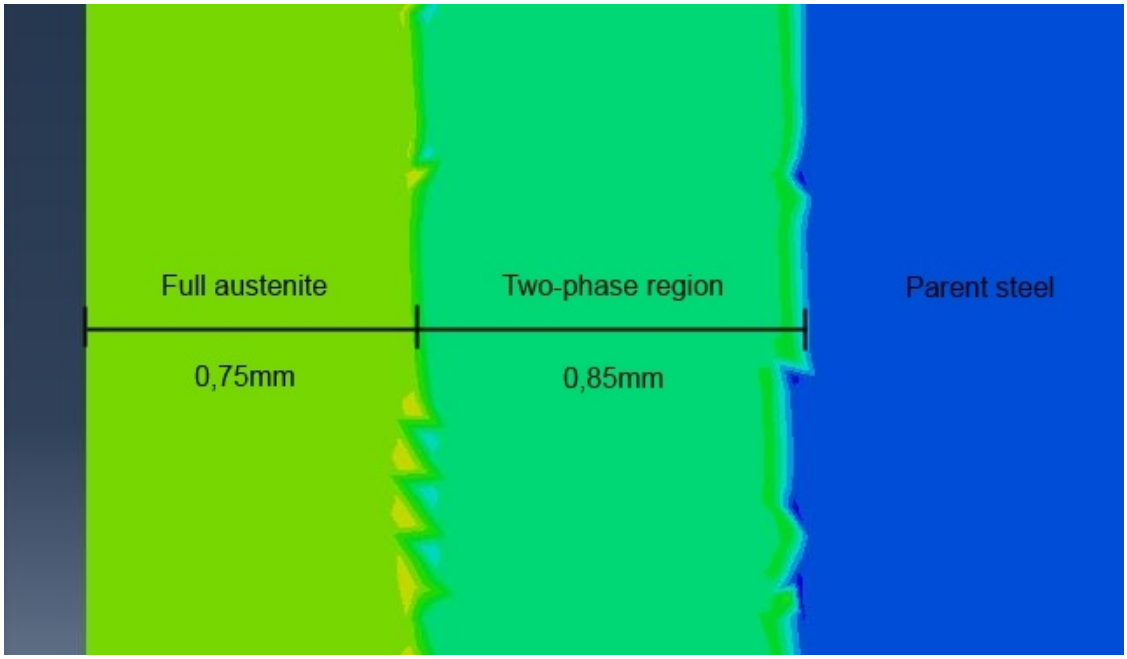

Figure 5.5. *Phase regions of 300mm/min flame-cutting for stress analysis.*

The thermal load applied to the surface is large in flame-cutting, as can be seen from the temperature curves in figures 5.1 and 5.2. The surface heats up to high temperatures in a matter of seconds and cools down to the martensite start temperature in a similar amount of time. From just a thermal point of view, an assumption can be made that the thermal shock from the applied heat will induce a great disparity in the stress distribution inside the part. The faster the cutting speed, the larger the thermal shock, and the differences in the temperature distribution.

5.2 Residual stresses

The main focus of this thesis was in finding out what happens inside the part while it is being flame-cut. The stress levels induced by the temperature differences are the desired output, which can be further analyzed if any yielding occurs. In this chapter the stress distribution results from the model are presented and the residual stresses are compared with the measured results from [33]. Also some temporary results essential to the development of the model are discussed.

The first objective for the model was to create a model which has all the material property values [see fig. 3.1-3.7] included and functions correctly from a thermal behavioral standpoint. The residual stress graphs for this model are presented in figure 5.6. It is worth mentioning that the phase transformations, especially martensite volume expansion, are not yet build into the model.

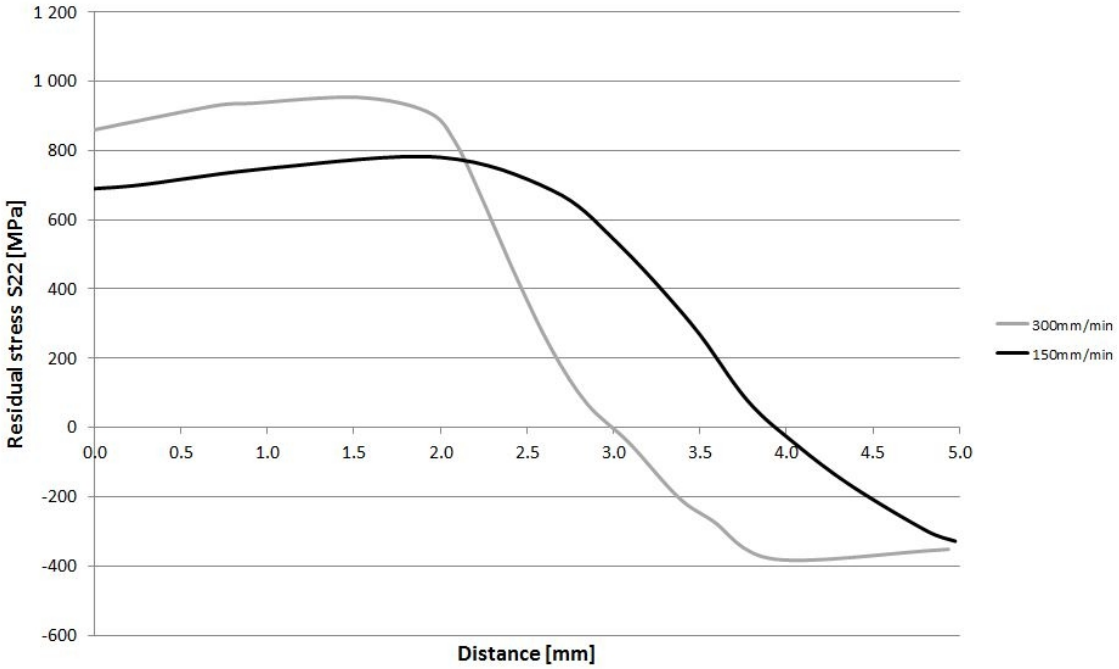

Figure 5.6. *Vertical residual stress curves of different cutting speeds without phase transformations.*

The residual stresses shown in figure 5.6 are a result of the plastic deformation occurring in high temperatures. Originally the part is at equilibrium at room temperature, but because of the thermal dilatation, the volume of the steel structure changes locally leading to plastic deformation. As the part cools down, it contracts, creating tensile stress to the deformed area while trying to reach the initial volume. This tensile stress is then balanced by compressive stress deeper inside the part, as can been seen from the curves.

Second goal for the model was to take the phase transformations into account. An adaptation of the martensite volume expansion was made and after a series of iterative calculations, a sufficient value for the isotropic axial expansion was found. The effects of the volume expansion of martensite are shown in figure 5.7, with the curves depicting the residual stresses of 300mm/min flame-cutting with and without the martensite phase transformation.

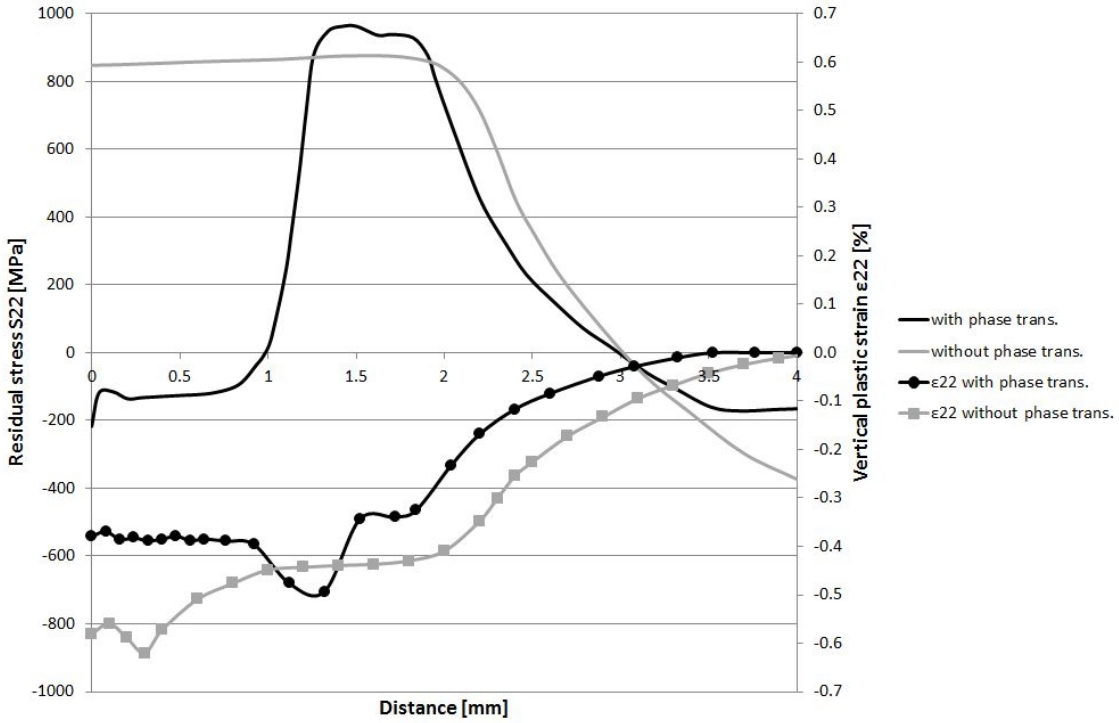

Figure 5.7. *Vertical residual stress curves illustrating the effect of martensite phase transformation for 300mm/min flame-cutting. Vertical plastic strain curves included.*

Curves in figure 5.7 shows, that the axial elongating deformation, which is connected to the martensite phase transformation, relieves the tensile stress from the surface, where the full austenite and part of the two-phase regions are located. The effect of the martensite transformation induced axial expansion value was studied, as three values were tried: 1%, 0.8% and 0.75%. The corresponding volume expansions are 3,03%, 2,42% and 2,27%, respectively. The residual stress graphs of these iterations are shown in figure 5.8.

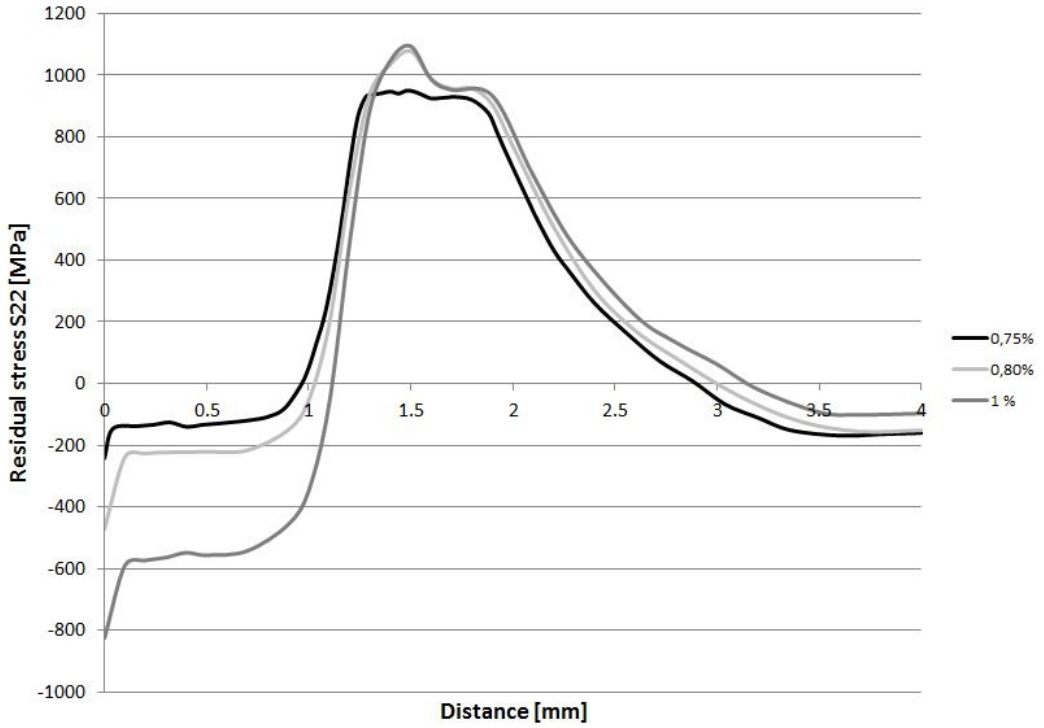

Figure 5.8. *Vertical residual stress curves of 300mm/min flame-cutting with different axial expansion parameters.*

The compressive stress at the surface is extremely sensitive to the value of the transformation induced axial expansion, as can be seen from figure 5.8. A change of 0.25 percentage unit in the axial expansion parameter creates a difference of over 400MPa in the full austenite region. The value of 0.75% was chosen for further calculations.

After the parameters for the model were chosen, desired data could be generated. One of the main objectives of this thesis was to find out what kind of stress levels occur during the flame-cutting process. In figure 5.9 are stress graphs of five different nodes from the middle line; the nodes are located at one millimeter intervals starting from the cut edge.

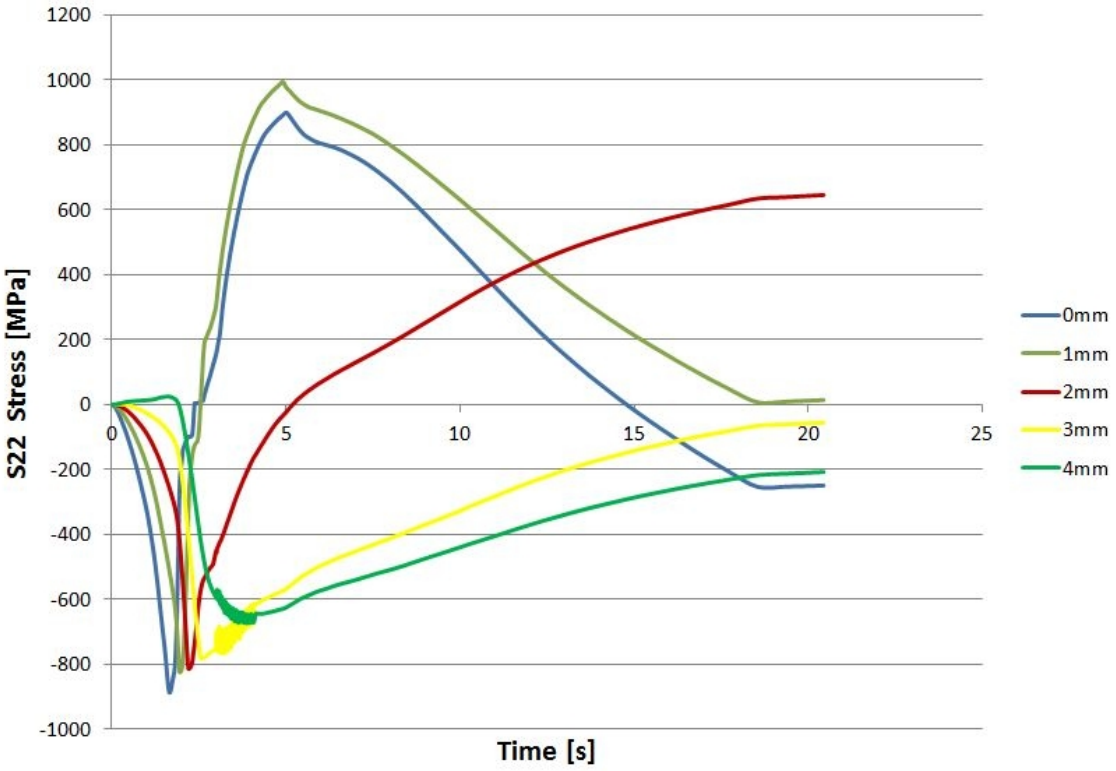

Figure 5.9. *Vertical (S22) stress during 300mm/min cutting as a function of time. Distances in the curve titles are from the cut edge.*

The stress curves from figure 5.9 show, that the heat from the flame creates compressive stress near the surface. The stress starts to turn to tensile, when the heat is no longer applied and the part begins cooling down after 3 seconds. The peak value of tensile stress is at 5 seconds, when the part has reached the M_s-temperature and martensite starts to form. The effect of the martensite nucleation can be seen from the 0mm and 1mm node stress curves, which are located in the phase transformation regions in figure 5.5. The node at 2mm instead is not located in the phase transformation regions, and therefore the tensile stress keeps continuously increasing until the part reaches room temperature. It is noteworthy that the maximum possible stress at a given temperature is limited by the current yield strength of the material. In figure 5.10 are the stress curves of 150mm/min flame-cutting with the same node selections.

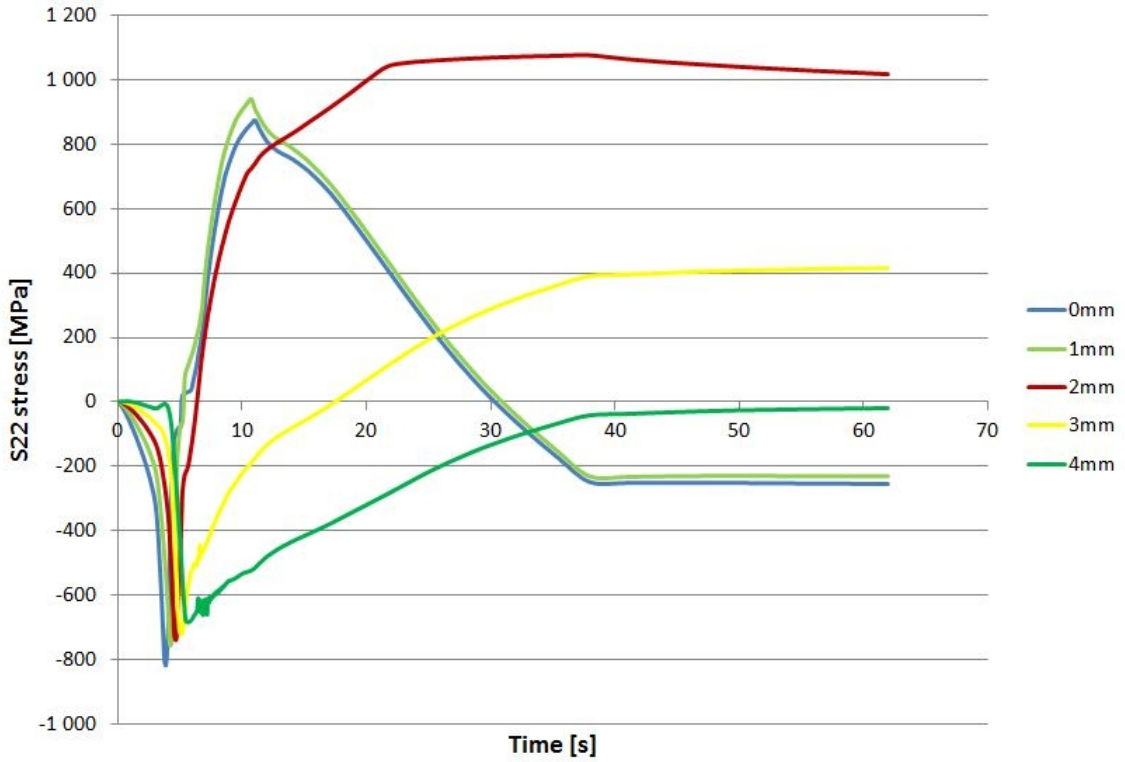

Figure 5.10. *Vertical (S22) stress during the 150mm/min cutting as a function of time. Distances in the curve titles are from the cut edge.*

The vertical stress curves for 150mm/min cutting resembles the ones for 300mm/min cutting. The martensite transformation eases the tensile stress and the peak value is located approximately at 2 millimeters and is over 1000MPa. The node is at this time at 350°C, so yielding might be possible, but definitely not certain. It is worth mentioning that the end of the stress curves are not yet residual stresses, as for example, the tensile stress in the 2mm curve keeps decreasing towards the value in figure 5.11, where are the residual stress curves presented for both 150mm/min and 300mm/min cutting with the respective vertical plastic strain curves.

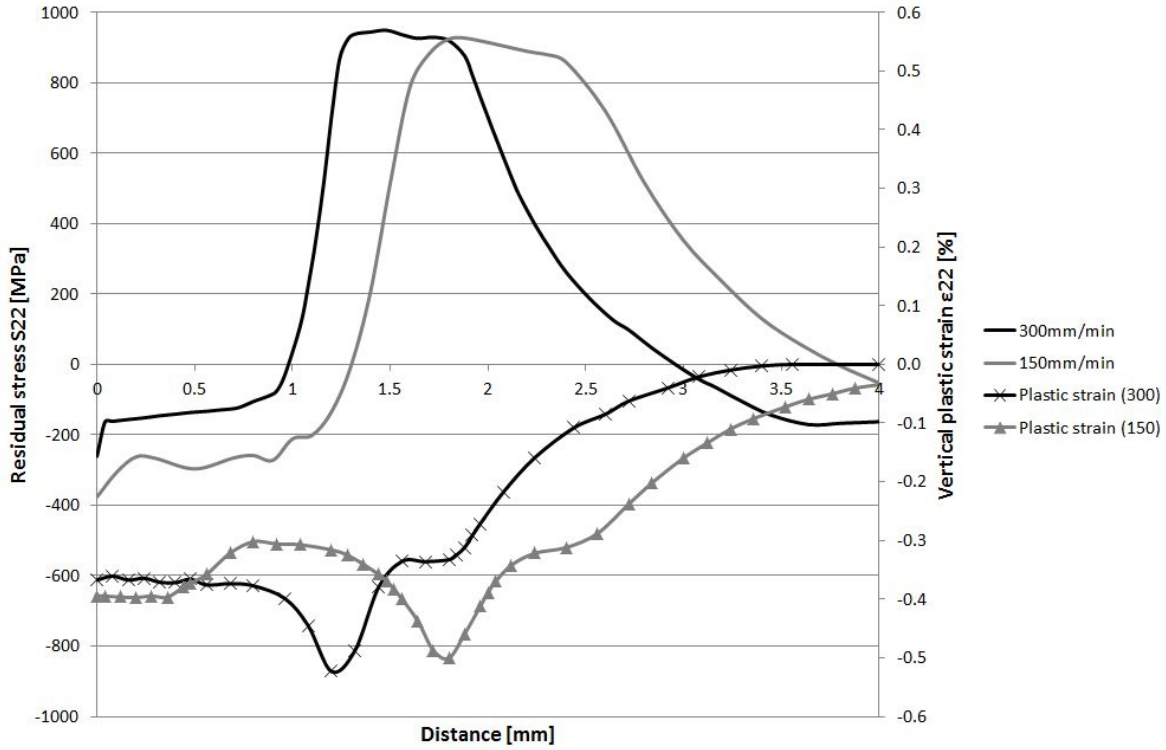

Figure 5.11. *Vertical residual stress and plastic strain curves of 150mm/min and 300mm/min cutting.*

The effect of plastic deformation can be clearly seen from figure 5.11, as the residual stress curves follow the plastic strain curves. For both cutting speeds, the tensile stress maximum exceeds 900MPa and it starts from the part of the two-phase region, where the austenite fraction is less than 30%. The middle of the stress peak is at the boundary between the two-phase region and parent steel. Because of this strict temperature boundary between the elements, some excess stress might occur due to the incapabilities of the model to simulate the behavior of parent steel at reasonably high temperatures, for example the tempering of residual martensite, which would affect the yield strength of the steel by lowering it [20]. This would lead to plastic deformation, which relieves tensile stress.

The shapes of the curves are quite similar, but the compressive stress area at the surface is larger for 150mm/min. This is a result of the longer exposure time of heat from the flame, so that the phase transformation regions are larger and more elements experience the elongating effect of the martensite transformation. To further explain the stress distribution inside the steel plate, than just from the middle line, in figure 5.12 is a picture of the computed stress fields.

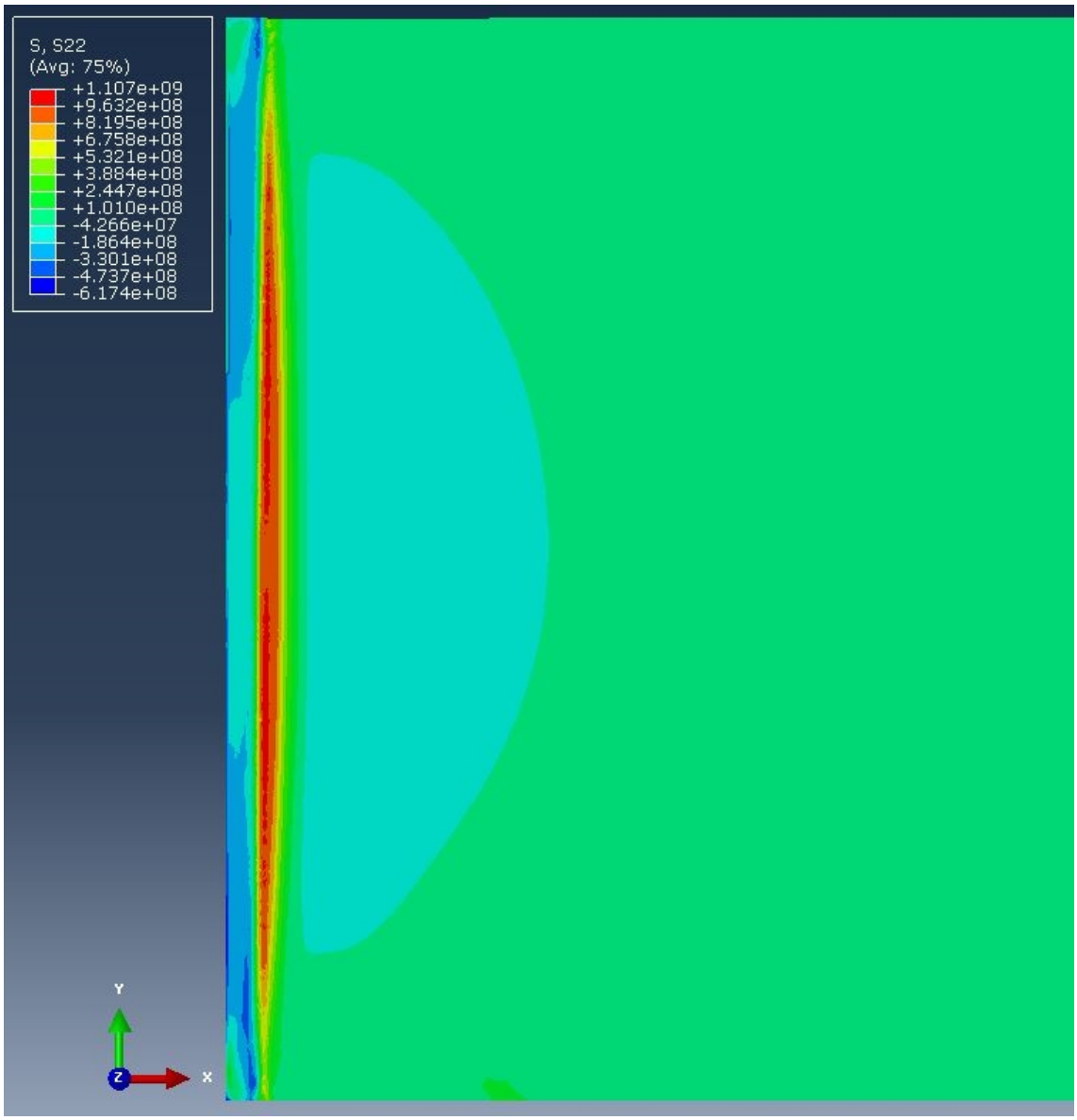

Figure 5.12. *Vertical residual stress distribution of the part for 300mm/min flame-cutting.*

The vertical residual stress distribution in figure 5.12 shows that the red colored tensile stress maximum locates at the same distance, which is approximately 1.5mm, throughout the part. At the up and bottom surfaces the vertical residual stress is zero, as is to be expected according to the laws of mechanics. The compressive stress region behind the tensile stress is there to balance the part to equilibrium, as discussed in subsection 3.3.2. The stress distribution of the part is similar to the one reported by Lindgren et al.[6] with the exception of maximum values.

Since the model was assumed to work sufficiently, more applications could be tested with it. Calculations for faster cutting speeds, as in 500mm/min and 1000mm/min, were made, and the results are presented in figure 5.13. The required heat load for both cutting speeds were iterated and the heat flux amplitudes adjusted according to the ratio between the respective cutting speeds and the cutting speed of 150mm/min.

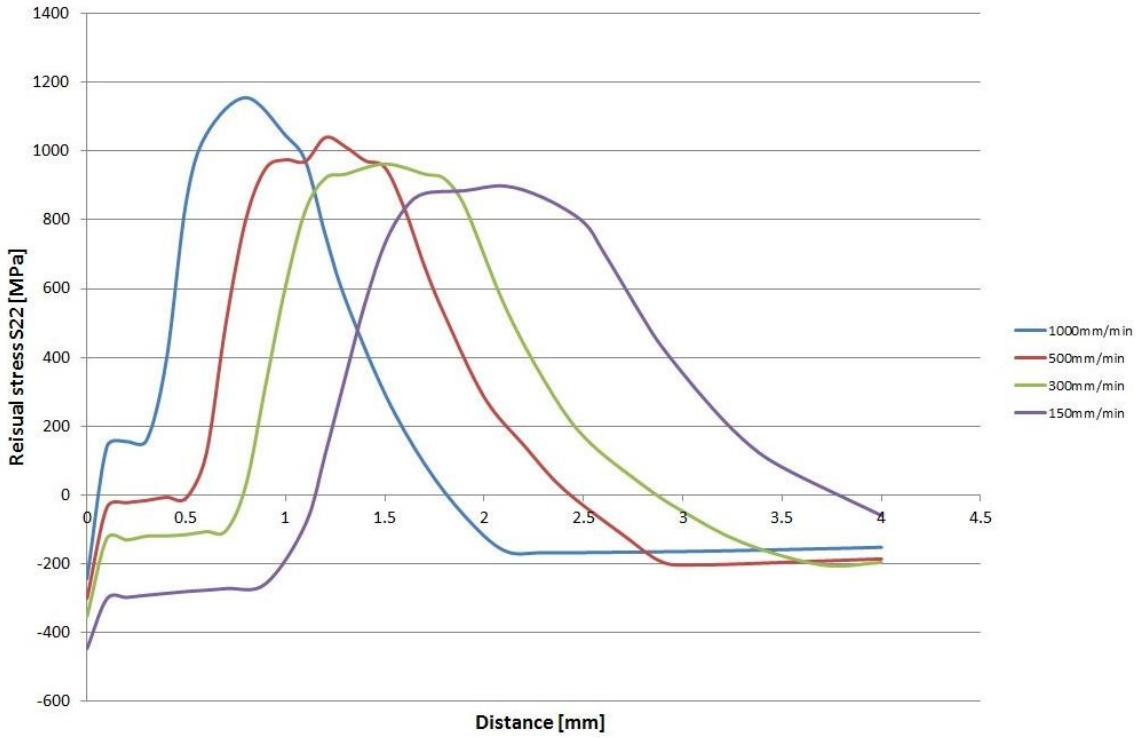

Figure 5.13. *Vertical (S22) residual stresses for different cutting speeds.*

As can be seen from figure 5.13, there is a clear linear development in the residual stress curves according to the cutting speed. Thermal shock from the flame is greater with higher cutting speeds, which results in greater tensile stress maximums nearer the surface. It appears that the volume expansion induced by the martensitic transformation is not enough to create compressive stress region to the surface in faster cutting speeds, as the vertical stress is around zero for 500mm/min cutting and tensile stress region appears for 1000mm/min cutting. With the 1000mm/min cutting, there is a risk of yielding, as the residual stress maximum is close to the yield strength value at room temperature shown in figure 3.7. A conclusion can be drawn from figure 5.13, that slower cutting speeds are safer in terms of possible yielding. But it is commonly known, that with lower cutting speeds, the hardness of the material decreases due to the longer heat exposure. Thus, more process optimization is required.

The residual stress distribution of steel plates with different thicknesses was one of the objectives for the model. Three steel plates; 20mm, 40mm and 60mm were cut with a cutting speed of 300mm/min and the residual stress curves from the middle line are presented in the following figure 5.14.

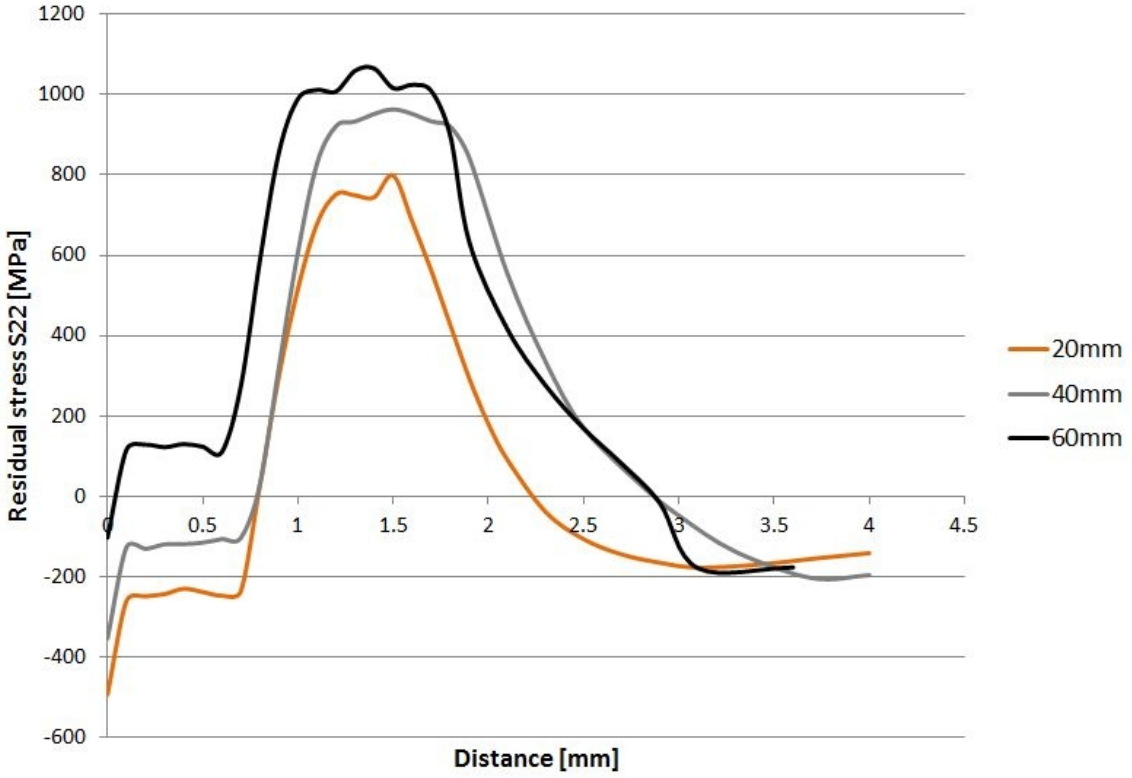

Figure 5.14. *Vertical residual stress curves of steel plates with various thicknesses. Cut with a cutting speed of 300mm/min.*

The curves in figure 5.14 show that the thickness of the steel plate has a major role in the development of the stress distribution. For thinner plates, the vertical deformation can happen more freely and even some bending might occur. This is not the case for thicker plates, since the deformation in the middle of the part is more restricted, which induces higher tensile stresses. The tensile stress peak increases with increasing thickness, and the compressive stress at the surface diminishes accordingly. A conclusion can be drawn that the cutting speed of 300mm/min is not suitable for cutting a 60mm thick steel plate, but for thinner plates it is a viable option. It is commonly known in the industry that thin steel plates do not crack, which agrees with the residual stress curves in figure 5.14.

Next application for the model was to study the effect of pre-heating, as it is noticed to lower the tensile stress maximums in residual stress measurements. The part was set to different temperatures as a predefined field and the heat flux magnitudes were adjusted, so that the surface elements would not exceed the melting temperature. Three new calculations were conducted by pre-heating the whole part to 100°C, 200°C and 300°C, then applying the heat flux and letting the part cool down to near room temperature. At this point, the stress state of the part did not noticeably change as function of time. The residual stress curves of these calculations are presented in figure 5.15 with the original room temperature curve.

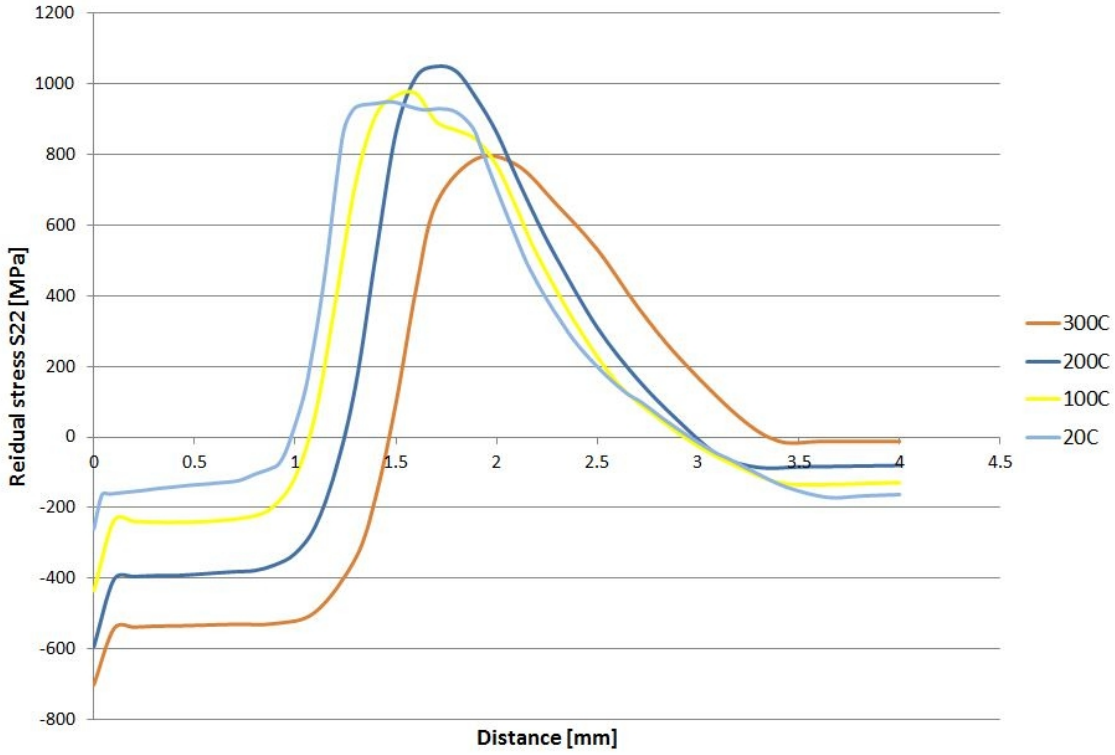

Figure 5.15. *Vertical residual stress curves of 300mm/min flame-cut pre-heated plate.*

By studying the stress curves of the pre-heated part in figure 5.15, it is clear that the pre-heating increases the compressive stress at the surface, and the compressive region extends deeper into the part. This is because the part is at uniform pre-heated temperature, so more elements reach the phase transformation temperatures when the heat is applied to the cut edge. The tensile stress peak in the 300°C graph is notably lower than in the other graphs, which is good from failure prevention perspective. The thermal shock to the 300°C steel has less effect, because the temperature differences inside the part are smaller and the yield strength [see fig. 3.7] starts rapidly decreasing at around 400°C.

Post-heat treatment was also one of the applications for the model. The simulation included the part to cool down for 5 minutes before heat was applied to the cut edge again. The magnitude of the heat was significantly lower and it was applied until the cut edge reached a temperature of 600°C. The results are presented in figure 5.16 as residual stress curves for the initial situation before the post-heat and after the treatment.

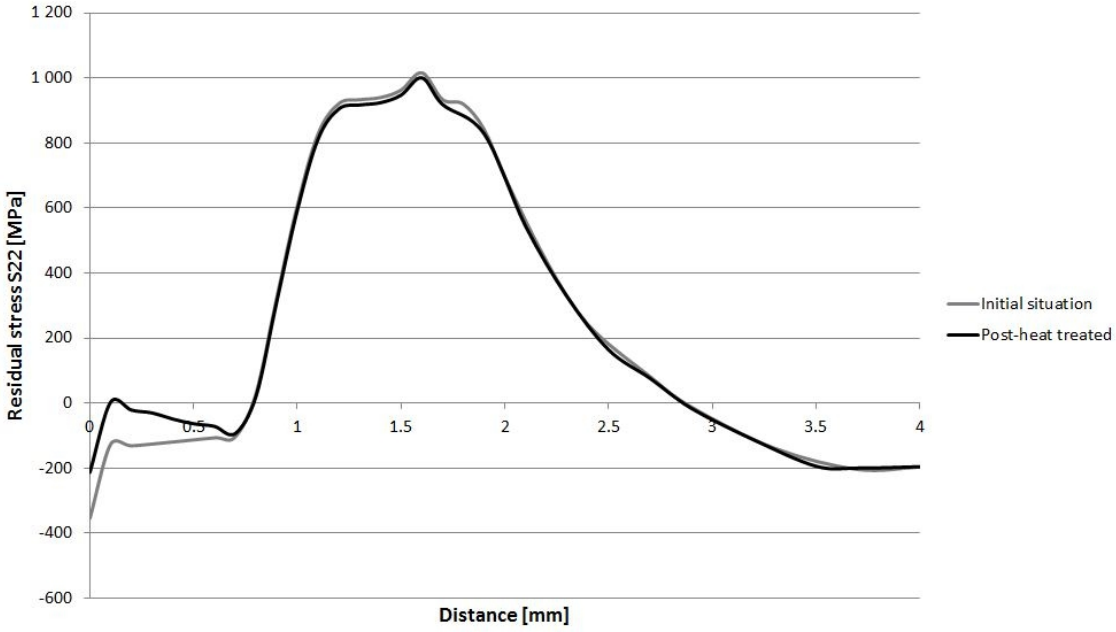

Figure 5.16. *Residual stress graphs of a post-heat treated part.*

It is obvious, that the model does not work for post-heat treatment, as can be seen from figure 5.16. The only change in the graphs is the decrease of the compressive stress at the surface. This is because the temperatures inside the part are not high enough for any plastic behavior to occur besides the surface, which means no changes to the stress distribution. Also the phase transformations are absent, as the maximum temperatures does not reach the A_1 temperature, and importantly, the tempering of martensite is not included in the model.

5.3 Model verification against experiments

In the final part of this chapter are the comparisons of results between the FEM simulations and the residual stress measurements conducted by [33]. The method used by [33] was based on non-destructive x-ray diffraction, and the results are presented as similar stress graphs to the ones created from the simulations. First graphs are of residual stresses of 150mm/min flame-cutting, which are shown in figure 5.17.

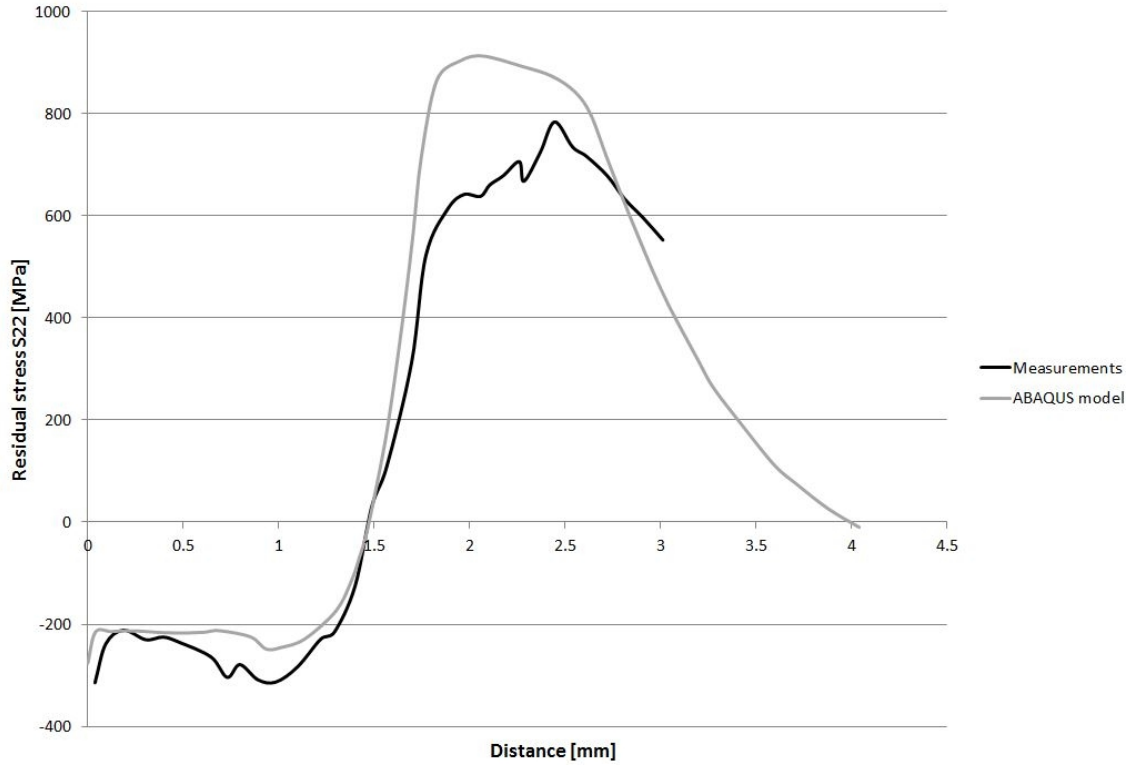

Figure 5.17. *The computed results compared with the measurements conducted by [33] for 150mm/min flame-cutting.*

The residual stress distributions for 150mm/min cutting are quite similar in the phase transformation regions, but start to differ after the tensile stress peak is surpassed. The measurements end at 3mm, but according to [33], the stress graph is supposed to intersect with the zero stress line (x-axis) at over 5mm. The tensile stress maximum is higher in the model, but that is to be expected, since the behavior of the material in the simulations is not totally equivalent to the behavior of steel in real life. As a conclusion, the model works well for 150mm/min cutting in the areas, which experience phase transformations. The comparison between the model and the measurements for 300mm/min flame-cutting is presented next in figure 5.18.

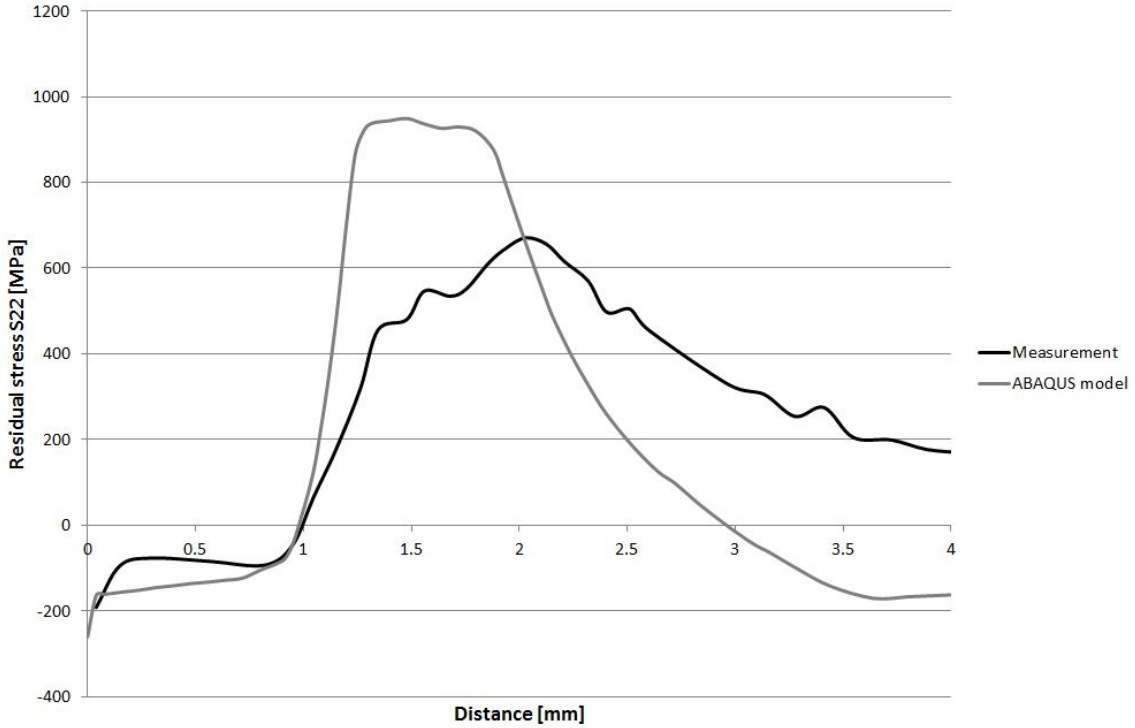

Figure 5.18. *The computed results compared with the measurements conducted by [33] for 300mm/min flame-cutting.*

As can be seen from figure 5.18, the differences between the residual stress curves of 300mm/min cutting are larger than with 150mm/min cutting; the tension peak of the model is about 300MPa higher and locates 0,5mm closer to the surface than in the measurements. In the measurements, the tensile stress region is distributed to a significantly longer area, which implies that the material behavior and the heat load in the model are not fully accurate.

Comparisons between the computed results and the measurements conducted by [33] for pre-heated specimens were also one of the initial objectives of the model. The curves for this are presented in figure 5.19. It should be noted that the conditions of the pre-heating may differ between the simulations and measurements.

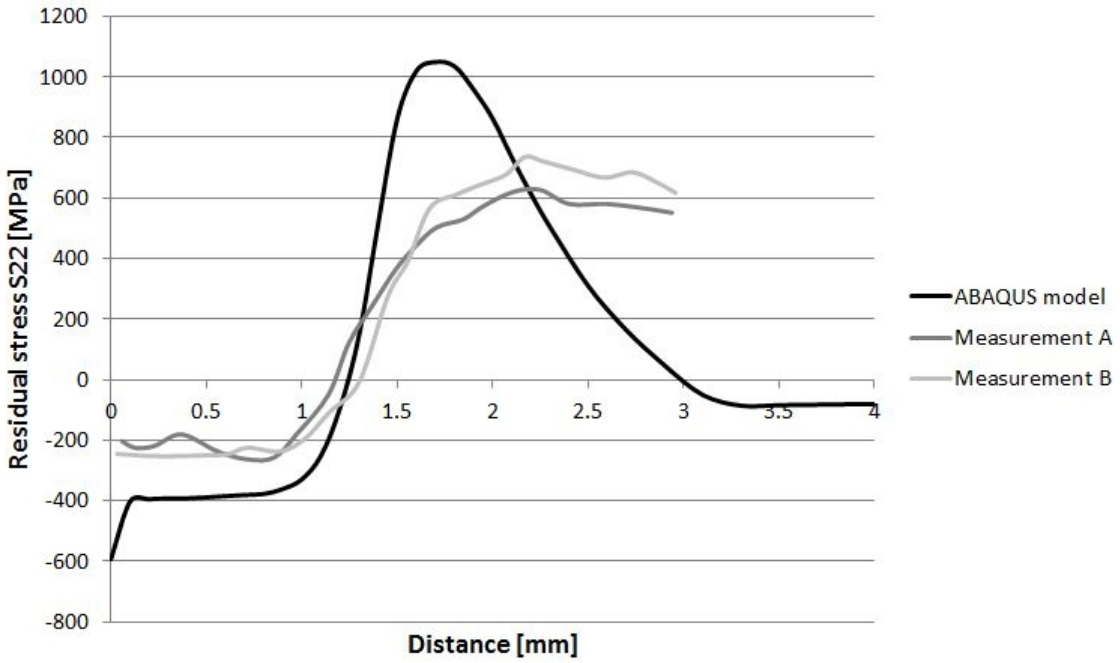

Figure 5.19. *The computed results of a 200°C pre-heated plate compared with the measurements conducted by [33] for 300mm/min flame-cutting.*

The residual stress curves of the FEM simulations and the measurements from figures 5.18 and 5.19 indicate that the pre-heating of the plate to 200°C has notable impact on the compressive stress region at the surface, which is a desired result. The differences between the curves for pre-heating in figure 5.19 are relatively similar to the differences in the stress curves for cutting without pre-heating in figure 5.18. An assumption can be made that the reasons behind these differences are also similar.

The residual stress results presented in this section are all vertical, because they are the ones that can be compared with the measurements. Because of the plane strain theory, the program also calculates the stresses along the cut edge (z-axis), but the heat from the flame is only applied from the x- and y-directions, which makes the results in z-axis less accurate. The residual stresses in the x-direction are close to zero throughout the part, as are the shear stresses at the middle line, making them negligible.

6. CONCLUSION

In this thesis, the flame-cutting of thick low-alloyed steel plates has been modelled. The purpose of the analysis was to assess the thermomechanical conditions inside the steel plate, both during and after the flame-cutting process. The model was created in a finite element program ABAQUS as two-dimensional for simplification reasons, and the input material was made to behave as similar to the studied steel as possible.

A variety of simulations were computed using the model, such as cutting with different cutting speeds, cutting of pre-heated and post-heated plate, and cutting of steel plates with different thicknesses. Martensitic and austenitic phase transformations were also included into the model by user subroutines. The results are presented mostly as vertical residual stress distributions along the middle line of the steel plate, but the results from the simulations of cutting speeds of 150 and 300mm/min are more closely analyzed. The 150mm/min flame-cutting is the initial simulation, to which the other simulations were based on.

The results from the simulations are generally good, and usable information about the conditions during the flame-cutting has been obtained. The residual stress distributions are relatively coincident with the experimental measurements at the phase transformation regions. The martensitic transformation creates a compressive stress region to the surface, as was initially assumed. The model works best for the application it was initially built for, which is with the cutting speed of 150mm/min. Further derivatives from this application increase the margin of error, due to the unique characteristics of each new application.

Due to the complex nature of flame-cutting, some simplifications had to be done in order for the model to work; the model was chosen to be simulated as two-dimensional and the flame-cutting process was implemented as a non-uniform time-dependent heat flux applied to the cut edge. These simplifications increased the factors of uncertainty. Good data could still be obtained by using the two-dimensional model, and the time savings were significant compared to three-dimensional simulation.

Based on the comparison between the simulations and the experimental measurements, it seems that the impact time of the flame is longer, because the tensile stress areas extend deeper into the part in the measurements than in the model. An assumption can be made that impact of the conducted heat from the flame before it arrives might be larger. Thus, revision of the time periods and magnitudes in the heat flux amplitude distribu-

tion would further improve the correspondence between the experimental and the numerical results.

Other suggestions for future study include creating a subroutine that takes different temperature histories of the material nodes into consideration. This would require a lot of material property measurements of the studied steel, but it would increase the accuracy even further. The tempering of martensite could be implemented to the model, which should decrease the tensile stress maximums and further improve the behavior of the material in the model. Also some of the constants used in the phase transformation calculations could be studied to match better with the alloy of steel at issue.

REFERENCES

[1] Hendricks B.R. 1999, Simulation of plasma arc cutting, M.Sc. thesis, Faculty of Engineering, Peninsula Technikon, p. 1-42.

[2] Jokiaho T. 2014, Lujien teräslevyjen polttoleikkausreunan karakterisointi - jäännösjännitykset ja niiden vaikutus halkeiluherkkyyteen., M.Sc. thesis, Tampereen Teknillinen Yliopisto, Tampere, pp. 101.

[3] Teräslevyjen terminen leikkaus. Helsinki 1985, Metalliteollisuuden Kustannus-Oy, ISBN 951-817-221-8, ISSN 0357-7368. Tekninen tiedotus.

[4] Metallirakentajan käsikirja. 2008, Hämeen ammattikorkeakoulu, Hämeenlinna, pp. 285.

[5] Thiébaud, R., Drezet, J-M., Lebet, J-P., 2013. Experimental and numerical characterization of heat flow during flame cutting of thick steel plates, vol. 214, Journal of Materials Processing Technology, p. 304-310.

[6] Lindgren, L.E., Carlestam, A., Jonsson, M., 1983. Computational model of flame-cutting. Journal of Engineering Materials and Technology 15, 440-445.

[7] Hansen, J.L. Numerical modeling of welding induced stresses. Ph.D. thesis. Technical University of Denmark 2003. Department of Manufacturing Engineering and Management, pp. 158.

[8] Iguchi, M., Ilegbusi, O.J. 2014. Basic Transport Phenomena in Materials Engineering. vol. 17, Springer eBooks, pp. 260.

[9] Lampinen, M.J. 1997. Termodynamiikan perusteet, book, Otatieto, Espoo, 182p.

[10] Mills, A.F. (1999). Basic heat and mass transfer, 2nd ed. ed., Prentice Hall, Upper Saddle River (NJ), 1000p.

[11] Ueda, Y., Murakawa, H., Ma, N. 2012. Welding deformation and residual stress prevention, book, Joining and Welding Research Institute, Osaka University. pp. 292.

[12] Outinen, H., Salmi, T. & Vulli, P. 2007. Lujuusopin perusteet, book, Pressus, Tampere, 464 p.

[13] ABAQUS Analysis user's manual, Version 6.13.

[14] Radaj, D. 1992. Heat Effects of Welding, Springer-Verlag, Berlin, Heidelberg. p 1-322.

[15] Shim, Y., Feng, Z., Lee, S., Kim, D., Jaeger, J., Papritan, J.C. & Tsai, C.L. 1992. Determination of Residual Stresses in Thick-Section Weldments, vol. 71, Welding research supplement, New York, p. 305-312.

[16] Callister, W.D.Jr. 2007. Materials science and engineering an introduction, book, 7th ed., John Wiley & Sons, New York, pp. 721.

[17] Martensitic structures, Metallography and Microstructures. 2004. ASM handbook, vol. 9, ASM international. p. 165-178.

[18] Bhadeshia, H.K.D.H. and Honeycombe, R.W.K. 2006. Steels – microstructure and propertis, 3rd edition, Elsevier Ltd, Oxford.

[19] Heat treating, 1991. ASM handbook vol. 4, ASM international.

[20] Porter, D.A. and Easterling, K.E. 1992. Phase Transformations in Metals and Alloys, book, 2nd ed., Chapman & Hall, London, pp. 439.

[21] K. Andrews, 1965. Empirical Formulae for the Calculation of Some Transformation Temperatures, *J. Iron Steel Inst.,* vol. 203, p 721–727

[22] A.R. Marder and G. Krauss, The Morphology of Martensite in Iron-Carbon Alloys, *Trans. ASM,* Vol 60, 1967, p 651–660

[23] Speer, J.G. and Gaster, R.J., 2013. Austenitizing in Steels, *Steel Heat Treating Fundamentals and Processes*. Vol 4A, *ASM Handbook*, ASM International, p 309–316.

[24] Cias, W.W. 1977. Austenite Transformation Kinetics of Ferrous Alloys, Climax Molybdenum Co., Greenwich, United States.

[25] Salmi, T., Virtanen, S. 2008. Materiaalien mekaniikka, Pressus Oy, Tampere, p. 21-113.

[26] Norton, R. L. 2010. Machine Design an Integrated Approach, 4th ed., Prentice Hall, New Jersey, USA.

[27] Leblond, J.B., Mottet, G., Devaux, J.C., 1986. A theoretical and numerical approach to the plastic behavior of steels during phase transformations—I. Derivation of general relations. J. Mech. Phys. Solids 34, 395–409.

[28] Taleb, L., Sidoroff, F., 2002. A micromechanical modeling of the Greenwood-Johnson mechanism in transformation induced plasticity, International Journal of Plasticity, Vol. 19(10), pp. 1821-1842.

[29] Denis, S. 1996. Considering stress-phase transformation interactions in the calculation of heat treatment residual stresses, Journal De Physique. IV : JP, Vol. 6(1), pp. C1-159-C1-174.

[30] Kamamoto, S., Nishimori, T., Kinoshita, S., 1985. Analysis of residual stress and distortion resulting from quenching in large low-alloy steel shafts, Kobe Steel Ltd, Kobe, Japan.

[31] Macedo, M.Q, Cota, A.B., Araújo, F. G.d.S, 2011. The kinetics of austenite formation at high heating rates, R. Esc. Minas, Ouro Preto, vol 64(2), pp. 163-167.

[32] Lindgren L.E., Carlestam A. 1993. An Improved Two-Dimensional Model of Flame-cutting, International Conference on Computer-Assisted Materials Design and Process Simulation, Tokyo, Japan, pp. 141-146.

[33] Jokiaho T. 2015. Personal communication.

[34] Clarke, K. 2008. The Effect of Heating Rate and Microstructural Scale on Austenite Formation, Austenite Homogenization, and As-Quenched Microstructure in Three Induction Hardenable Steels, Ph.D. thesis, Colorado School of Mines.

[35] Saunders, N., Guo, U.K.Z., Li, X., Miodownik A.P., Schillé, J. –Ph. 2003. Using JMatPro to model materials properties and behavior, The Journal of The Minerals, vol. 55(12), Metals & Materials Society, pp. 60-65.

APPENDIX A: USER SUBROUTINE CODE

```
C    Arttu Laitinen – User subroutine for the simulation of
C    flame cutting

C    Subroutine for the marking of elements which reach the
C    phase transformation temperatures

     SUBROUTINE USDFLD(FIELD,STATEV,PNEWDT,DIRECT,T,CELENT,
     &    TIME,DTIME,CMNAME,ORNAME,NFIELD,NSTATV,NOEL,NPT,LAYER,
     &
     KSPT,KSTEP,KINC,NDI,NSHR,COORD,JMAC,JMATYP,MATLAYO,LACCFLA)
C
     INCLUDE 'ABA_PARAM.INC'
C
     CHARACTER*80 CMNAME,ORNAME
     CHARACTER*3 FLGRAY(15)
     DIMENSION FIELD(NFIELD),STATEV(NSTATV),DIRECT(3,3),
     &  T(3,3),TIME(2)
     DIMENSION ARRAY(15),JARRAY(15),JMAC(*),JMATYP(*),COORD(*),
     &  TEMP(15)

C    Formatting the variables

     INTEGER ONE, ZERO
     double precision TEMP_OLD, DTEMPPI, A1, A3, Ms, Mf
     double precision alfa_aust, steel, alfa1, alfa2, alfa3,
     double precision alfa_mart, beta, TRIP_mart, f_m, f_a, tau

     ZERO = 0
     ONE = 1
     A1 = 1018.
     A3 = 1350.
     Ms = 713.
     Mf = 507.

C    Subroutine obtains the temperature information and flags
C    the elements as 0, 1 or 2 according to at which temperature
C    range they are

        CALL GETVRM('TEMP',TEMP,JARRAY,FLGRAY,JRCD,JMAC,JMATYP,
     &   MATLAYO,LACCFLA)

C    SDV(3) is temperature change and SDV(7) is the
C    heating/cooling rate

     TEMP_OLD = STATEV(2)
     DTEMPPI = TEMP(1) - TEMP_OLD
     STATEV(3) = DTEMPPI
     STATEV(7) = DTEMPPI/DTIME

C    SDV(1) is the flag for the temperature ranges
C    (T < A1 = 0, A1 < T < A3 = 1, A3 < T < molten = 2 and
C    molten < T = 3)
```

```
      IF ((TEMP(1) .LT. A1) .AND. (STATEV(4) .EQ. ZERO)) THEN
      STATEV(1) = 0.D0

       ELSE IF ((TEMP(1) .GE. A1) .AND. (TEMP(1) .LT. A3) .AND.
(STATEV(4) .EQ. ZERO)) THEN
      STATEV(1) = 1.D0
      STATEV(4) = ONE

       ELSE IF ((TEMP(1) .GE. A3) .AND. (TEMP(1) .LT. 1790.)
.AND. (STATEV(5) .EQ. ZERO)) THEN
      STATEV(1) = 2.D0
      STATEV(5) = ONE

       ELSE IF ((TEMP(1) .GT. 1790.) .AND. (STATEV(6) .EQ. ZERO))
THEN
      STATEV(1) = 3.D0
      STATEV(6) = ONE

      END IF

C     SDV(13) is the maximum temperature

      IF (TEMP(1) .GT. STATEV(2)) THEN
      STATEV(13) = TEMP(1)

      END IF

      STATEV(2) = TEMP(1)

C     This sentence tells ABAQUS which material properties to use
C     according to the direction of the temperature change.
C     Field = 1 if cooling and Field = 2 if heating

      IF (STATEV(1) .LT. 3.D0) THEN

           IF (DTEMPPI .GE. 0.) THEN
           FIELD(1) = 2

           ELSE IF (DTEMPPI .LT. 0.) THEN
           FIELD(1) = 1

           END IF

      ELSE IF (STATEV(1) .EQ. 3.D0) THEN
      FIELD(2) = 3

      END IF

      return
      end
```

```
C     Thermal expansion subroutine to include the phase
C     transformations to the calculations

      SUBROUTINE UEXPAN(EXPAN,DEXPANDT,TEMP,TIME,DTIME,PREDEF,
     & DPRED,STATEV,CMNAME,NSTATV,NOEL)
C
      INCLUDE 'ABA_PARAM.INC'
C
      CHARACTER*80 CMNAME
C
      DIMENSION EXPAN(*),DEXPANDT(*),TEMP(2),TIME(2),PREDEF(*),
     & DPRED(*),STATEV(NSTATV)

      double precision TEMP_OLD, DTEMPPI, A1, A3, Ms, Mf
      double precision alfa_aust, steel, alfa1, alfa2, alfa3,
      double precision TRIP_mart, beta, f_m, alfa_mart, f_a, tau

C     alfa_aust and steel are thermal expansion coefficients

      alfa_aust = 2.0d-5
      steel = 1.3d-5

      A1 = 1018
      A3 = 1350.
      Ms = 713.
      Mf = 507.

C     f_m is the phase fraction of martensite calculated by
C     using a modified koistinen-marburger equation
C     f_a is the phase fraction of austenite calculated by
C     using the Weibull cumulative distribution function

C     TRIP_mart is the adaptation of the total axial expansion
C     induced by the martensitic transformation
C     alfa_mart is the expansion coefficient during the
C     martensitic phase transformation (between Ms-Mf)

      TRIP_mart = (0.0075/(Mf-Ms))
      beta = -0.04
      f_m = 1.0 - EXP(-0.04*(Ms-TEMP(1)))
      alfa_mart = (((1.0-f_m)*alfa_aust + f_m*steel) + TRIP_mart)
      tau = (STATEV(13)-A1)/(A3-A1)
      f_a = 1.0 - EXP(-6.0*(tau**2))

      STATEV(11) = alfa_mart
      STATEV(12) = f_m
      STATEV(14) = f_a
      STATEV(16) = tau

C     IF-sentences for the thermal expansion coefficient.
C     Many different situations are taken into account where the
C     thermal expansion coefficient may vary. It is dependent on
C     the austenite and martensite phase fractions, current
C     temperature and the flag which the element has been given.
```

```
      IF ((STATEV(1) .EQ. 2.D0) .AND. ((TEMP(1) .LE. Ms) .AND.
(TEMP(1) .GT. Mf))) THEN
     EXPAN(1) = alfa_mart*TEMP(2)

      ELSE IF ((STATEV(1) .EQ. 1.D0) .AND. ((TEMP(1) .LE. Ms)
.AND. (TEMP(1) .GE. Mf))) THEN
     EXPAN(1) = (f_a*alfa_mart*TEMP(2)) + (1-f_a)*steel*TEMP(2)

      ELSE IF (((TEMP(1) .GE. A1) .AND. (TEMP(1) .LT. A3)) .AND.
(STATEV(1) .EQ. 1.D0)) THEN
     EXPAN(1) = f_a*alfa_aust*TEMP(2) + (1-f_a)*steel*TEMP(2)

      ELSE IF (((TEMP(1) .LT. A1) .AND. (TEMP(1) .GT. Ms)) .AND.
(STATEV(1) .EQ. 1.D0)) THEN
     EXPAN(1) = f_a*alfa_aust*TEMP(2) + (1-f_a)*steel*TEMP(2)

      ELSE IF (TEMP(1) .GE. A3) THEN
     EXPAN(1) = alfa_aust*TEMP(2)

      ELSE IF (((TEMP(1) .LT. A3) .AND. (TEMP(1) .GT. Ms)) .AND.
(STATEV(1) .EQ. 2.D0)) THEN
     EXPAN(1) = alfa_aust*TEMP(2)

      ELSE
     EXPAN(1) = steel*TEMP(2)
      END IF

C    State variables for verifying that the code works

     STATEV(8) = TEMP(2)
     STATEV(9) = EXPAN(1)
     STATEV(10) = EXPAN(1)/TEMP(2)
     STATEV(15) = f_a*alfa_aust*TEMP(2) + (1.0-
f_a)*steel*TEMP(2)

      return
      end
```